BACHELOR THESIS

submitted to the

Combined Faculties for the Natural Sciences and for Mathematics
of the Ruperta-Carola University of Heidelberg

for the degree of

Bachelor of Natural Sciences

Put forward by

Finn A. Schmutte

born in
Hannover

2020

Closed Optical Cycle Scheme for Absorption Imaging of ^{39}K Atoms at Intermediate Magnetic Field Strengths

This Bachelor Thesis has been carried out by Finn Schmutte at the
Kirchhoff-Institute for Physics in Heidelberg
under the supervision of
Prof. Dr. Markus K. Oberthaler

Zusammenfassung

Diese Bachelorarbeit behandelt ein bildgebendes System für ultrakalte Kalium Atome. Eine neuartige Methode zur Abbildung wird diskutiert, welche durch theoretische Überlegungen über die Natur der möglichen Zerfallskanäle motiviert ist. Ausgehend von der Betrachtung der Dipolmatrixelemente mit angelegtem statischen Magnetfeld wird die zugehörige Mastergleichung konstruiert und numerische Simulationen zur Optimierung von Streuprozessen im atomaren Medium durchgeführt, welche auch experimentell untersucht werden. Das resultierende geschlossene Viernievausystem wird im Populationsgleichgewicht mit einem effektivem Zweiniveausystem indentifiziert. Zuletzt wird die Kalibration des Systems diskutiert, welche eine präzise Bestimmung der atomaren Dichteverteilung erlaubt.

Abstract

This bachelor thesis treats the imaging of ultra-cold potassium atoms. A new imaging method is employed, which is motivated by theoretical considerations on the nature of possible decay channels. The master equation is constructed from the dipole matrix elements in presence of magnetic fields and numerical simulations are executed to optimize scattering events, which are compared to experimental findings. The resulting closed four-level system is identified in the steady state limit with an effective two-level system. Finally, a calibration technique of the imaging system is examined, which allows for a precise determination of the atomic density distribution.

Contents

Introduction

For the study of quantum many-body systems, there has been a surge in interest for well-controlled experimental systems. With the rise of advanced cooling techniques for dilute atomic gaseous samples [1] Bose-Einstein condensation was achieved [2][3], which provides a powerful subject for investigations on the nature of quantum behaviour in macroscopic systems. Remarkably, Bose-Einstein condensates can be described as coherent quantum matter fields, wherefore the inherent quantum attributes dictate the behaviour of the complete condensate. In mean-field approximation a non-linear differential equation, the Gross-Pitaevskii equation (GPE), is used to describe the behaviour of the system. Since classical computing methods lack the performance to compute time dynamics of complex quantum mechanical systems we perform physical computing. A precisely controllable initial condition can be evolved with respect to time, such that we can execute simulation, that exceed the mean-field approximation. Our system therefore solves equations, which otherwise would not be efficiently solvable by current numerical means. More specifically, we exploit a broad Feshbach resonance of the potassium isotope $^{39}\mathbf{K}$ [4] in order to tune the interaction strength of the system, which can therefore be modulated by an external homogeneous magnetic field. Furthermore, the environment of the condensate is variable due to a tunable optical trapping potential. Thus the experiment can be used to map the dynamics of structural formations, that obey the evolution of the Gross-Pitaevieskii equation, but more interestingly the experiment incorporates beyond mean-field effects and delivers a basis to investigate far from equilibrium physics [5]. Since Bose-Einstein condensation can occur in three dimensions one could in principle study physical phenomena here, in the experiment however we can manipulate the density distribution. With the installation of a digital micromirror device (DMD) a plethora of positional distributions in three or less dimensions as initial conditions will be realisable [6]. In order to evaluate the evolved systems state, we use absorption imaging, where we exploit the energy level structure of potassium atoms.

In this thesis we will take a closer look into the imaging system used to investigate ultra-cold potassium atoms. Especially, we will discuss problems that arise due to the complex energy structure of potassium atoms at intermediate magnetic fields. We will confer upon the dipole matrix elements that follow from considerations on a suitable set of basis vectors, that describe the electronic wavefunction. With knowledge about all possible decay modes we are going to write down the Hamiltonian for the atom photon interaction, that is needed to capture the imaging process. Starting from this Hamiltonian we will construct the Lindblad master equation, in order to include spontaneous decays phenomenologically. Consequently, we present a possible way to obtain a closed four-level imaging scheme and perform simulations on the number of scattered photons, which is used to optimize the ratio between a binary laser imaging system. Our ultimate goal is to present a technique, with which we can elongate imaging times and increase scattering events during imaging. Finally, we will briefly describe a possible calibration for this setup and argue for a precise determination of the atomic density.

Chapter 1

Theoretical Framework

1.1 Bose Einstein Condensation

First, we will begin our theoretical discussion of imaging ultra-cold atomic samples by giving a brief outline on Bose-Einstein condensates (BEC). BECs are sometimes referred to the fifth state of matter and is the central object of study in our experiment. Bose-Einstein condensation occurs when particles, that obey Bose statistics, reach a critical phase space density of $\rho_{crit} \geq 2.612$, in this instance he thermal de-Broglie-wavelength λ_{dB} is on the order of the typical interparticle spacing [7]. Further, it entails a plethora of phenomenona that ought to be studied, as it is a many-body system, that despite its scale inhibits a significant amount of quantum attributes. A BEC can be described as a quantum matter field, rather than a classical gas in the framework of statistical thermodynamics. Interestingly a BEC consists of Bosons, that occupy the same state, i.e. the ground state of the system and unite to a coherent ensemble of particles, or to stay in the language of quantum fields, a coherent field of matter. This fact has many implications on the system, e.g. that the entirety of the condensate can be treated as one collective wavefunction. In the following we want to elaborate shortly on the main conclusions drawn from qunatum field theory (QFT). The Hamiltonian of the condensate is given by [8]:

$$\hat{\mathcal{H}} = \sum_{ij} \mathcal{H}_{ij}^{\mathrm{sp}} \hat{a}_i^\dagger \hat{a}_j + \frac{1}{2} \sum_{ijkm} \langle ij|\hat{V}|km\rangle \hat{a}_i^\dagger \hat{a}_j^\dagger \hat{a}_k \hat{a}_m \tag{1.1}$$

Where $\hat{a}_i$ and $\hat{a}_i^\dagger$ are the creation and annihilation operators respectively, that obey the Bose commutation rules $[\hat{a}_i, \hat{a}_j^\dagger] = \delta_{ij}$ and $[\hat{a}_i, \hat{a}_j] = [\hat{a}_i^\dagger, \hat{a}_j^\dagger] = 0$, $\langle ij|\hat{V}|km\rangle$ is the matrix element of the interaction potential $\hat{V}(\mathbf{r})$ between particles and $\mathcal{H}_{ij}^{\mathrm{sp}}$ is the matrix elements of the single-particle Hamiltonian, which is given by:

$$\mathcal{H}_{ij}^{\mathrm{sp}} = \int \mathrm{d}^3\mathbf{r} \tilde{\Phi}_i^*(\mathbf{r}) \hat{\mathcal{H}}^{\mathrm{sp}} \tilde{\Phi}_j(\mathbf{r}) \tag{1.2}$$

here we introduced the state wavefunctions $\tilde{\Phi}_i(\mathbf{r})$ and the single-particle Hamiltonian is defined via the trap potential V_{trap}:

$$\mathcal{H}^{\text{sp}} = -\frac{\hbar}{2m}\nabla^2 + V_{\text{trap}} \tag{1.3}$$

From the Hamiltonian all relations can be calculated, but we only want to present one prominent result, which is the Gross-Pitaevieskii equation (GPE). One can arrive at this formula by defining the Bose field operators $\hat{\Psi}^\dagger(\mathbf{r}) = \sum_i \hat{a}_i^\dagger \tilde{\Phi}_i^*(\mathbf{r})$ and $\hat{\Psi}(\mathbf{r}) = \sum_i \hat{a}_i \tilde{\Phi}_i(\mathbf{r})$ and employing a mean field approximation. In order to stay concise we will only show the outcome here:

$$i\hbar\frac{\partial}{\partial t}\psi(\mathbf{r},t) = \left(-\frac{\hbar^2\nabla^2}{2m} + V_{\text{trap}}(\mathbf{r}) + U_0|\psi(\mathbf{r},t)|^2\right)\psi(\mathbf{r},t) \tag{1.4}$$

This formula is written in terms of the complex function $\psi(\mathbf{r},t)$, that is the expectation value of the Bose field operator $\psi(\mathbf{r},t) \equiv \langle\hat{\Psi}(\mathbf{r},t)\rangle$, which is also referred to as the order parameter of the system. Further we have defined the parameter $U_0 \equiv 4\pi\hbar^2 a/m$, which considers only low energy binary particle-particle collisions, such that s-wave scattering dominates over p-wave or d-wave scattering. s-wave scattering described by the scattering length a.

The GPE can be thought of as the non-linear Schrödinger equation, which is not far-fetched, as Eq. 1.4 reduces to said equation for $U_0 = 0$. Moreover, it is noteworthy, that the a Bose-Einstein condensate is still complex enough, such that it can produce plenty of phenomena even in mean-field approximation. The Gross-Pitaevskii equation, should nonetheless therefore be regarded essential to our experiment.

1.2 Feshbach Resonances

Since we wish to modulate the interaction strength of the bosonic field, which is represented in Eq. 1.4 by $U_0 = 4\pi\hbar^2 a/m$, we may do so by changing the s-wave scattering length a. In the experiment we have chosen the isotope $^{39}\mathbf{K}$ not only because it can be treated as an integer spin particle, i.e. a boson, but also because it provides a broad Feshbach resonance, where the scattering length can be tuned by an external magnetic field.

Feshbach resonances occur in many-body systems with exceptionally low kinetic energies, such as BECs. Due to two-body collisions unstable molecule-like bound states form. In ultracold system scattering reduces to s-wave scattering [9], which can be parametrized around a Feshbach-resonance as:

$$a(B) = a_{bg}\left(1 - \frac{\Delta B}{B - B_0}\right) \tag{1.5}$$

where B_0 is the position of the resonance, ΔB is the resonance width and a_{bg} is the background scattering length. It should be noted that this formula is only valid on proximity to a Feshbach resonance and describes a magnetically tuned resonance. Other forms of manipulation are possible, e.g. by optical methods.

For magnetically tuned Feshbach resonances to occur, a difference in magnetic momenta between the composite state and individual atoms is required. Since the magnetic field couples

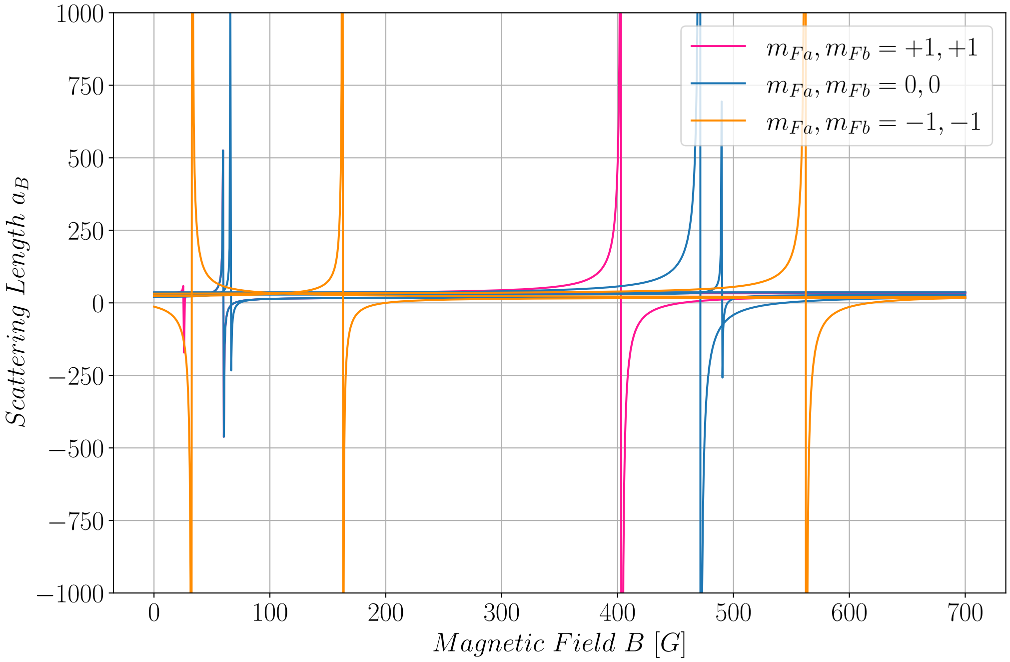

Figure 1.1: ***Feshbach Resonances between 0 and 700G of ^{39}K.*** *The color coded resonances correspond to a specific combination of substates in the F-basis for a binary resonance between atoms labeled a and b.*

to these momenta, the energy of the coupled state can be tuned. In literature [10], the occurrence of Feshbach resonances is often argued via molecular potential curves, where a energetically open channel is given by the background potential $V_{bg}(r)$ and closed channel $V_c(r)$, that describes bound states. In case of bipartite scattering with energy E, a Feshbach resonance appears when the molecular state of the closed channel comes close to the scattering state in the entrance channel.

1.3 Properties of ^{39}K

1.3.1 Hyperfine Structure

Despite the rather broad Feshbach resonance at $B = 562G$ an advantage of the potassium isotope ^{39}**K** is the single valence electron, which dramatically simplifies the energy substructure of the atom. More specifically the electronic configuration is $1s^2 2s^2 2p^6 3s^2 3p^6 4s^1$, such that all inner orbitals are filled and cause a shielding effect on the nucleus electromagnetic field. Usually calculation would be difficult, but for this reason we can treat the nuclear charge in good approximation as an effective charge Z_{eff} and also account for quantum defects, which capture the discrepancy to an effective hydrogen spectrum. Moreover the total spin $\hat{\mathbf{S}}$ and electronic angular momenta $\hat{\mathbf{L}}$ of the inner orbitals add to zero. Hence the only contribution comes form the valence electron and we define for the latter the total angular momentum $\hat{\mathbf{J}}$

as:

$$\hat{\mathbf{J}} = \hat{\mathbf{L}} + \hat{\mathbf{S}} \tag{1.6}$$

The quantum number J can take all values possible from the vector sum of Eq. 1.6: $|L - S| \leq J \leq L + S$. The corresponding energy splitting is the so-called fine structure. This however, is not the only way the energy levels are split. Further coupling between the nuclear spin $\hat{\mathbf{I}}$ and the total angular momentum $\hat{\mathbf{J}}$ causes the hyperfine structure with:

$$\hat{\mathbf{F}} = \hat{\mathbf{J}} + \hat{\mathbf{I}} \tag{1.7}$$

Similarly the respective quantum number F is between $|J - I| \leq F \leq J + I$. The nuclear spin for ^{39}**K** is $I = 3/2$ and will be treated fixed in this thesis, as we will not force nuclear transitions in the experiment. In the ground state $4^2S_{1/2}$ $L = 0$ and $S = 1/2$, whereas the first excited state $4^2P_{1/2}$ with $L = 1$ and the secondary is $4^2P_{3/2}$. The most significant transition between $(4^2S_{1/2} \rightarrow 4^2P_{1/2})$ is the $D1$-line and the transition $(4^2S_{1/2} \rightarrow 4^2P_{3/2})$ is the $D2$-line. In terms of the quantum number F the ground state for $J = 1/2$ is $F = 1, 2$, for states with $J = 3/2$ we have $F = 0, 1, 2, 3$, which are displayed in Fig. 1.2. In order to illuminate the underlying energy level structure in more detail, we are interested in the Hamiltonian of system. The latter can be determined by evaluating [11]:

$$\mathcal{H}^{\text{hfs}} = \sum_k \mathbf{T}^{(k)} \cdot \mathbf{M}^{(k)} \tag{1.8}$$

where $\mathbf{T}^{(k)}$ and $\mathbf{M}^{(k)}$ are spherical tensors of rank k, which describe the electronic and nuclear interaction. Since the $k = 0$ term is not specific to the hyperfine structure, we will discard it. However the $k = 1$ term is more interesting as it describes the magnetic dipole interaction of the nuclear magnetic moment with the magnetic field created by the electron. Since all further moments of the multipole expansion have minor contributions to the energy, we will only consider contributions up to quartic order. As the involved calculation is rather lengthy and has already been calculated by [12], we only present their result:

$$\hat{\mathcal{H}}^{\text{hfs}} = \frac{a_{\text{hfs}}}{\hbar^2}\hat{\mathbf{I}} \cdot \hat{\mathbf{J}} + \frac{b_{\text{hfs}}}{\hbar^2}\frac{3(\hat{\mathbf{I}} \cdot \hat{\mathbf{J}})^2 + \frac{3}{2}(\hat{\mathbf{I}} \cdot \hat{\mathbf{J}}) - \hat{\mathbf{I}}^2\hat{\mathbf{J}}^2}{2I(2I-1)J(2J-1)} \tag{1.9}$$

1.3.2 Zeeman Effect

Since we want to study the behaviour of a BEC in presence of a magnetic field, because we wish to modulate the interaction strength of the condensate via Feshbach resonances, we must account for the presence of the external force in our Hamiltonian. To this end we may treat the action of the magnetic field as first order perturbation of $\hat{\mathcal{H}}^{\text{hfs}}$, such that we can write the combined Hamiltonian as:

$$\hat{\mathcal{H}}^{tot} = \hat{\mathcal{H}}^{\text{hfs}} + \hat{\mathcal{H}}^{Z}, \tag{1.10}$$

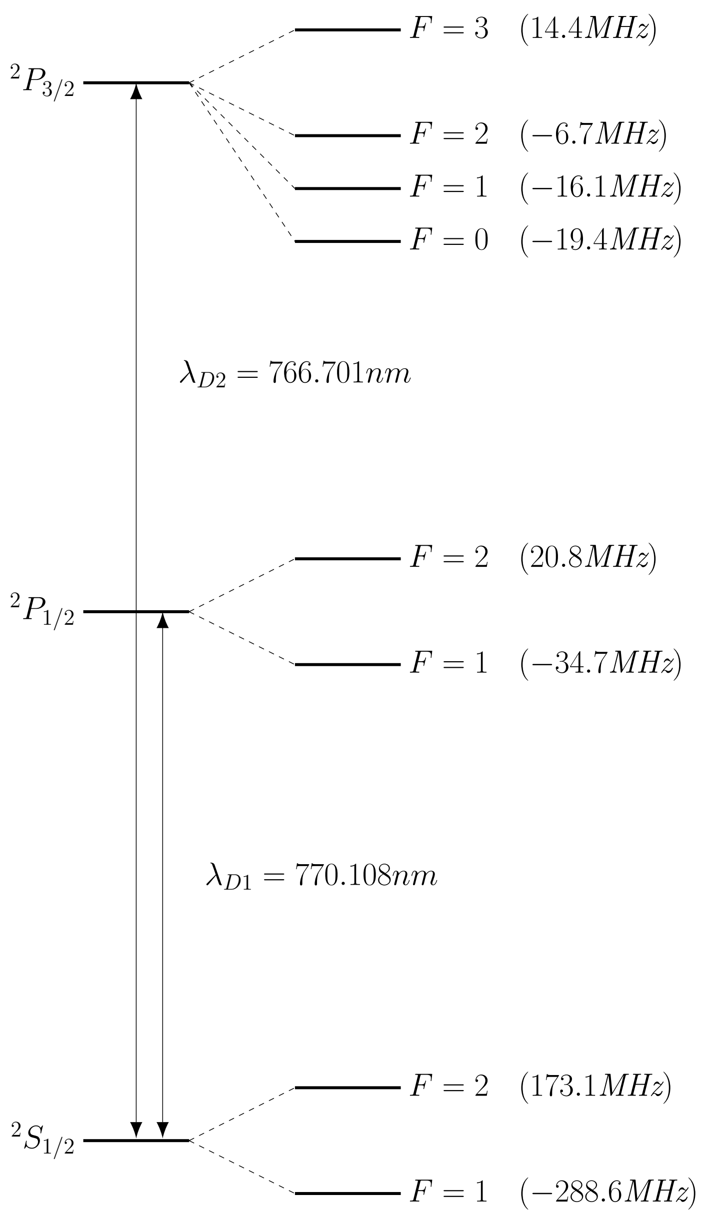

Figure 1.2: ***Energy structure of ^{39}K at zero magnetic field*** *consisting of D_1-line with $\lambda_{D_1} = 770.108nm$ and D_2-line $\lambda_{D_2} = 766.701nm$. Throughout this thesis the manifold of $^2S_{1/2}$ will be labeled as ground state, $^2P_{1/2}$ as intermediate state and $^2P_{3/2}$ as excited state. On the right side each respective hyperfine submanifold with degeneracy $2F+1$. To each substate a frequency is assigned, that denotes the shift from the according fine structure energy level.*

where the Zeeman contribution $\hat{\mathcal{H}}^Z$ is given by:

$$\hat{\mathcal{H}}^Z = (1/\hbar)\left(\mu_B g_J \hat{\mathbf{J}} + \mu_N g_I \hat{\mathbf{I}}\right) \cdot \mathbf{B} \tag{1.11}$$

In order to evaluate the combined Hamiltonian, one can either treat the appearing operators $\hat{\mathbf{L}}, \hat{\mathbf{S}}, \hat{\mathbf{J}}, \hat{\mathbf{I}}$ as operations on separate Hilbert spaces, such that the dot product in Eq. 1.9 translates to the tensor product, or one can choose a suitable basis and exploit the well known action of the operators on said basis vectors.

To gain more insight into the fundamental mechanics of angular momenta, it is fruitful to convince one self, that the orbital angular momenta span a Lie algebra on $\mathfrak{so}(3)$ [13]. Mathematically all possible products and linear combinations together with the commutator relation $[\hat{J}_i, \hat{J}_j] = i\hbar\epsilon_{ijk}\hat{J}_k$, where $(\{x, y, z\} \leftrightarrow \{i, j, k\})$, and the abstract unity $\mathbb{1}$ combine to the Lie algebra. Remarkably each element of the corresponding Lie group can be recovered by applying the exponential to an element of Lie algebra on $\mathfrak{so}(3)$. Finally this group can be identified with $SO(3)$ which is the special orthogonal group on $\mathbb{R}^3$.

By further stating, that $\hat{\mathbf{J}}^2 = \hat{J}_x^2 + \hat{J}_y^2 + \hat{J}_z^2$, we can deduce that $[\hat{J}_i, \hat{\mathbf{J}}^2] = 0$. Therefore each basis element $\hat{J}_i$ commutes with $\hat{\mathbf{J}}^2$, which is the so-called Casimir operator. Hence, a complete and shared set of orthonormal eigenvectors exists for the Casimir operator and $\hat{J}_z$. In the following we will denote these eigenvectors with $|J, m_J\rangle$, where m_J is the respective magnetic quantum number. To keep m_J dimensionless we introduce Planck's reduced constant $\hbar$, which also preserves the fact, that angular momenta have the dimension of an action. Subsequently we can formulate the effects of $\hat{J}_z$ and $\hat{\mathbf{J}}^2$ on said eigenvectors by:

$$\hat{J}_z |J, m_J\rangle = \hbar m_J |J, m_J\rangle \tag{1.12}$$

$$\hat{\mathbf{J}}^2 |J, m_J\rangle = \hbar^2 J(J+1) |J, m_J\rangle \tag{1.13}$$

Here $\hat{J}_z$ is the z component of the vector operator $\hat{\mathbf{J}}$, which can be interchanged with any angular momentum operator, as all relations are satisfied by this group of operators. The action of Eq. 1.13 produces diagonal elements and since $\hat{J}_z$ can not be diagonalized simultaneously with $\hat{J}_{x,y}$ it is often times more convenient to use the ladder operators $\hat{J}_+$ and $\hat{J}_-$, which are defined by $\hat{J}_\pm \equiv \hat{J}_x \pm i\hat{J}_y$ and create off-diagonal elements according to:

$$\begin{aligned} \hat{J}_+ |J, m_J\rangle &= \hbar\sqrt{(J - m_J)(J + m_J + 1)}\, |J, m_J + 1\rangle \\ \hat{J}_- |J, m_J\rangle &= \hbar\sqrt{(J + m_J)(J - m_J + 1)}\, |J, m_J - 1\rangle \end{aligned} \tag{1.14}$$

Eq. 1.13,1.14 will not be derived in the frame of this thesis, nonetheless one can be referred to [13] to gain more understanding on the topic.

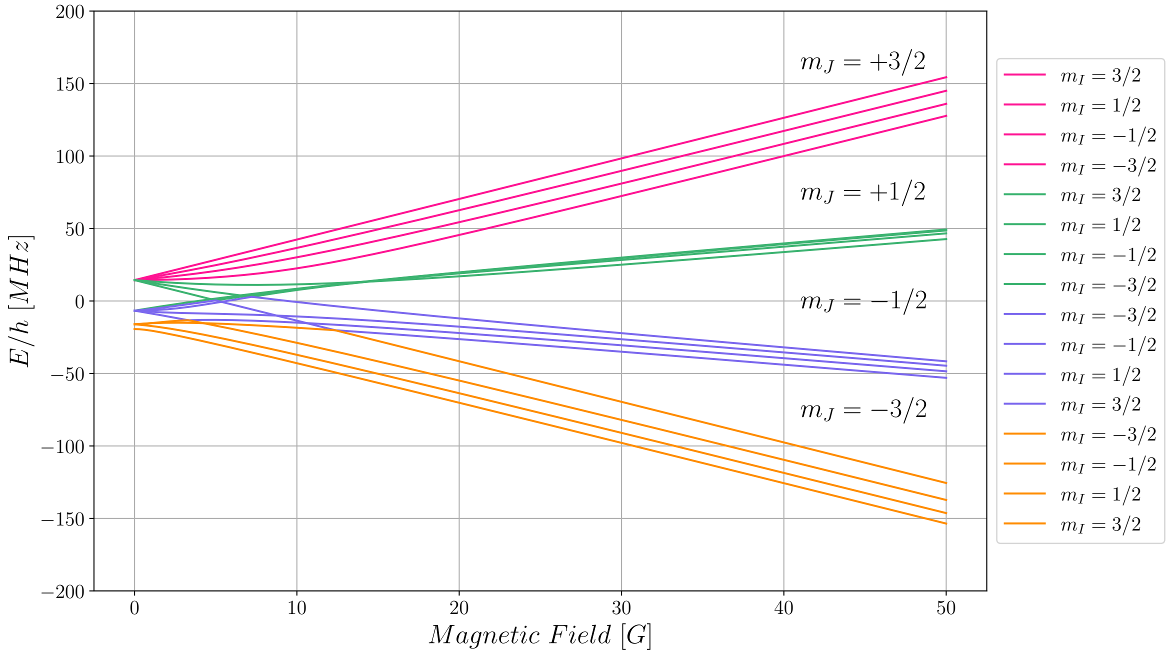

(a) *Energy splitting for excited state manifold* $^2P_{3/2}$

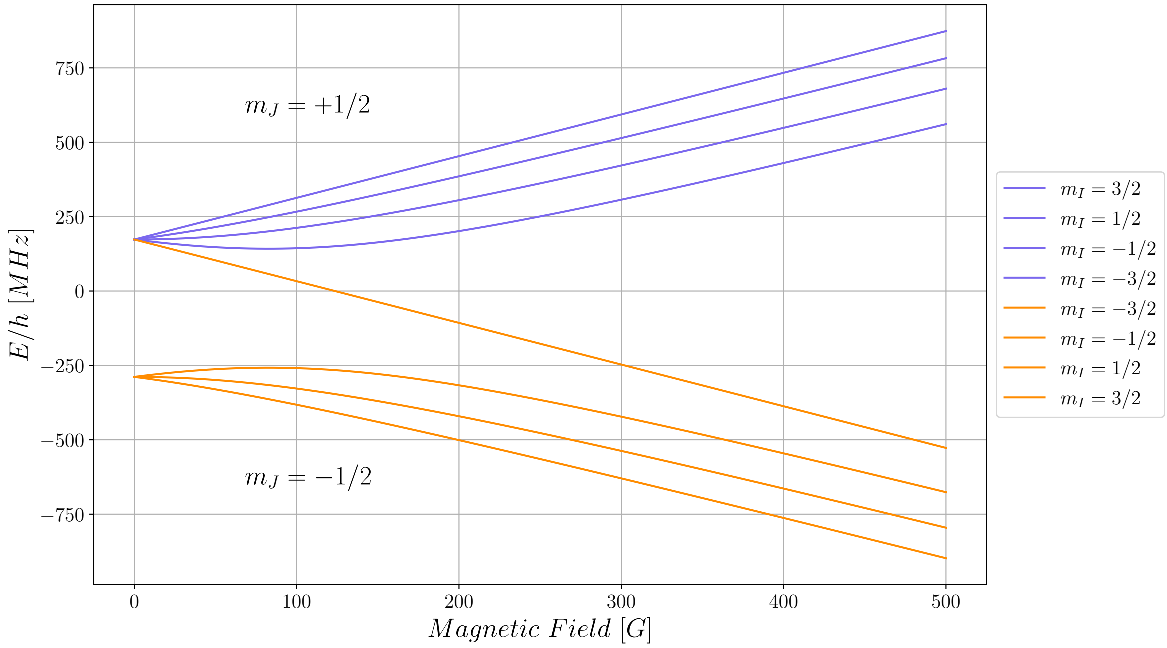

(b) *Energy splitting for ground state manifold* $^2S_{1/2}$

Figure 1.3: ***Breit-Rabi diagrams for*** $^2P_{3/2}$ ***and*** $^2S_{1/2}$ ***manifolds.*** *Lifting of degenarcy is portrayed for energy eigenvalues of the excited state* $^2P_{3/2}$ ***(a)*** *and ground state* $^2S_{1/2}$ ***(b)*** *manifold in presence of magnetic fields. The energy eigenbasis* F, m_F *is decoupled due to Zeeman splittings into groups of* m_J*, which together with* m_I *represent good quantum numbers for very high fields. The final ordering of* m_I *substates is not yet completed for the portrayed field strengths. The energyeigenvalues are calculated using tensor representation of the involved operators. Diagonalizing the Hamiltonian yields the shown Breit-Rabi diagrams.*

For the special case of Potassium $^{39}\mathbf{K}$ we calculate the energy eigenvalues for the excited state of the $D2$-line $4^2P_{3/2}$, which consists of 16 substates. The effect of an external magnetic field to the energy levels is typically named Zeeman effect, whose discoverer (Pieter Zeeman in 1896) recorded the energy splitting of spectral lines [14]. For $^{39}\mathbf{K}$ this splitting is portrayed in Fig. 1.3. At null field a good set of quantum numbers is given in the F, m_F-basis. Already at relatively low field strengths this basis ceases to provide a good set of quantum numbers, which is to say that the operators to an arbitrary set of eigenvectors do not commute with the Hamiltonian, i.e. the time evolution becomes non-trivial. By diagonalizing in the J, I-basis, the eigenvectors contain the coefficents for a change of basis in to the eigenbasis of Eq. 1.10. Consequently, the ordinary approach, meaning that we describe energy eigenstates in the F, m_F-basis, could be applied here, but would over-complicate the problem. Furthermore we observe a decoupling of $\hat{\mathbf{J}}$ and $\hat{\mathbf{I}}$ into four disjoint groups ordered by J and internally by I for the excited state and two groups for the ground state.

1.4 Dipole Matrix Elements

For now we have only discussed the internal energy structure of potassium. Here we will examine the dipole matrix elements of Potassium $^{39}\mathbf{K}$ more closely, which determine which decays are possible and quantify the probabilities with which these electronic decays do occur. Considerations on the dipole matrix elements will enable us to further understand the nature of interaction between atoms and photons.

As argued before it is of interest to study the atomic cloud at non-negligible magnetic fields. If we consider the Hamiltonian from Sec. 1.3.2 we are faced with two problems. The first is, that there are not always analytical solutions to the energy eigenstates. Moreover, in the intermediate magnetic field regime most atomic states will not be pure energy eigenstates, but compositions of multiple eigenstates. The latter poses a significant problem, as this means, that there are a manifold of decay modes, which are not covered in our theory by remaining in the F,m_F- basis. We must consider the states as the superposition and compute the dipole matrix elements accordingly to obtain correct results.

We will start by introducing the Wigner-Eckart theorem [15] and its power for calculating the dipole matrix elements. The theorem states, that for any spherical tensor $T_q^{(k)}$ the matrix element, when expressed in terms of the eigenstates of the angular momentum operator fulfills the following equation:

$$\langle \alpha j m | T_q^{(k)} | \alpha' j' m' \rangle = (-1)^{2k} \langle \alpha j | \mathbf{T}^{(k)} | \alpha' j' \rangle \langle j m \mid j' m'; k q \rangle \tag{1.15}$$

Here α contains all radial quantum numbers and j is a generalized angular momentum qunatum number with corresponding magnetic quantum number m_j. k denotes the tensor rank and q the q-th component of the tensor, in our case the polarisation state of the photon. An important notation is the reduced matrix element $\langle \alpha j | \mathbf{T}^{(k)} | \alpha' j' \rangle$, which no longer depends on m_j and is thereby considered to be reduced. The theorem allows us to fully separate the angular momentum part of the dipole matrix element from the radial part. Since all information on the linewidth is contained in the radial part, we must determine the angular momentum part, as it dictates the probability of any given decay. We will try to keep the formulae general and thus only identify $T_q^{(k)}$ with the dipole operator in the end. Our states $|\Psi\rangle$ are, as already mentioned, superpositions of all eigenstates of the basis $\mathcal{B}$:

$$|\Psi\rangle \equiv \sum_{p=1}^{\#\mathcal{B}} \mathcal{C}_p |\alpha; J^p m_J^p; I^p m_I^p\rangle \tag{1.16}$$

where $\#\mathcal{B}$ is the length of our basis and $\mathcal{C}_p$ are the weights of each contributing eigenstate. The excited state is given by:

$$\langle\Psi'| \equiv \sum_{b=1}^{\#\mathcal{B}'} (\mathcal{C}'_b |\alpha'; J'^b m'^b_J; I'^b m'^b_I\rangle)^\dagger \tag{1.17}$$

Thus we can evaluate the action of an operator:

$$\widetilde{\widetilde{T_q^{(k)}}} \equiv \widetilde{T_{q(\alpha,J)}^{(k)}} \otimes \mathbb{1}_{(I)} \equiv T_{q(\alpha,L)}^{(k)} \otimes \mathbb{1}_{(S)} \otimes \mathbb{1}_{(I)}, \tag{1.18}$$

such that $\widetilde{\widetilde{T_q^{(k)}}}$ only acts upon the Hilbert space spanned by the quantum numbers α and L. This is not done by chance, but because we deliberately want to maintain the characteristics of the dipole operator, which does not change the spin or its projection. Now we can write:

$$\langle\Psi'|\widetilde{\widetilde{T_q^{(k)}}}|\Psi\rangle = (\sum_{b=1}^{\#\mathcal{B}'} (\mathcal{C}'^*_b \langle\alpha'; J'^b m'^b_J; I'^b m'^b_I|)) \underbrace{(\widetilde{\widetilde{T_q^{(k)}}}(\sum_{p=1}^{\#\mathcal{B}} \mathcal{C}_p |\alpha; J^p m_J^p; I^p m_I^p\rangle))}_{*_1} \tag{1.19}$$

For now we only consider the right side of Eq. 1.19 $*_1$:

$$*_1 = \sum_{p=1}^{\#\mathcal{B}} \mathcal{C}_p (\widetilde{T_{q(\alpha,J)}^{(k)}} \otimes \mathbb{1}_{(I)})(|\alpha; J^p m_J^p\rangle \otimes |I^p m_I^p\rangle) \tag{1.20}$$

$$= \sum_{p=1}^{\#\mathcal{B}} \mathcal{C}_p \sum_{k,q} |\tilde{\alpha'}, kq\rangle\langle kq|J^p m_J^p; k'q'\rangle \otimes |I^p m_I^p\rangle \tag{1.21}$$

Where we made use of the Wigner-Eckart theorem in Eq. 1.21. By now returning to our original formula we yield:

$$(\sum_{b=1}^{\#\mathcal{B}'} (\mathcal{C}'^*_b \langle\alpha'; J'^b m'^b_J; I'^b m'^b_I|))(\sum_{p=1}^{\#\mathcal{B}} \mathcal{C}_p \sum_{k,q} |\tilde{\alpha'}, kq\rangle\langle kq|J^p m_J^p; k'q'\rangle \otimes |I^p m_I^p\rangle) \tag{1.22}$$

$$(\sum_{b=1}^{\#\mathcal{B}'} \sum_{p=1}^{\#\mathcal{B}} \mathcal{C}'^*_b \langle\alpha'; J'^b m'^b_J; I'^b m'^b_I|(\mathcal{C}_p \sum_{k,q} |\tilde{\alpha'}, kq\rangle\langle kq|J^p m_J^p; k'q'\rangle \otimes |I^p m_I^p\rangle)) \tag{1.23}$$

$$(\sum_{b=1}^{\#\mathcal{B}'}\sum_{p=1}^{\#\mathcal{B}}\mathcal{C}_b'^{*}\mathcal{C}_p\langle\alpha'; J'^{b}m_J'^{b}|(\sum_{k,q}|\tilde{\alpha}', kq\rangle\langle kq|J^{p}m_J^{p}; k'q'\rangle\otimes\langle I'^{b}m_I'^{b}|I^{p}m_I^{p}\rangle)) \tag{1.24}$$

$$(\sum_{b=1}^{\#\mathcal{B}'}\sum_{p=1}^{\#\mathcal{B}}\mathcal{C}_b'^{*}\mathcal{C}_p\langle\alpha'; J'^{b}m_J'^{b}|\tilde{\alpha}', J'^{b}m_J'^{b}\rangle\langle J'^{b}m_J'^{b}|J^{p}m_J^{p}; k'q'\rangle\langle I'^{b}m_I'^{b}|I^{p}m_I^{p}\rangle) \tag{1.25}$$

$$(\sum_{b=1}^{\#\mathcal{B}'}\sum_{p=1}^{\#\mathcal{B}}\mathcal{C}_b'^{*}\mathcal{C}_p(-1)^{-2k}\langle\alpha' J'^{b}||\widetilde{\widetilde{\widetilde{\mathbf{T}^{(k)}}}}||\alpha J^{b}\rangle\langle J'^{b}m_J'^{b}|J^{p}m_J^{p}; k'q'\rangle\delta_{I'^{b},I^{p}}\delta_{m_I'^{b}m_I^{p}}) \tag{1.26}$$

This result reflects the proposition, that $\widetilde{\widetilde{\widetilde{T_q^{(k)}}}}$ only acts on the angular momentum Hilbert space, as the Kronecker deltas forbid a magnetic spin flip. We must however, further reduce this statement since J is the composition of L and S, and since the operator $\widetilde{\widetilde{\widetilde{T_q^{(k)}}}}$ does not couple to the Hilbert space of S either, we can further reduce the matrix element $\langle\alpha' J'^{b}||\widetilde{\widetilde{\widetilde{\mathbf{T}^{(k)}}}}||\alpha J^{b}\rangle$. The calculations here fore follow closely to [16] and represent the action of tensor operator on one component. Because we do not know the effect of $\widetilde{\widetilde{\widetilde{\mathbf{T}^{(k)}}}}$ on the composite state J, we perform a change of basis, using the well known Clebsch-Gordon coefficients, into the uncoupled basis of L and S. Here we can apply the Wigner-Eckart theorem from Eq: 1.15:

$$\begin{aligned}
\langle J'\|\widetilde{\widetilde{\widetilde{\mathbf{T}_q^{(k)}}}}\|J\rangle &= (-1)^{2k}\sum_{m_J q}\langle J'm_J'|\widetilde{\widetilde{\widetilde{T_q^{(k)}}}}|Jm_J\rangle\langle J'm_J' \mid Jm_J; kq\rangle \\
&= (-1)^{2k}\sum_{\substack{m_J q\\ m_L' m_S' m_L m_S}}\langle J'm_J' \mid L'm_L'; S'm_S'\rangle\langle L'm_L'; S'm_S'|\widetilde{\widetilde{\widetilde{T_q^{(k)}}}}|Lm_L; Sm_S\rangle\langle Lm_L; Sm_S \mid Jm_J\rangle \\
&\qquad \times\langle J'm_J' \mid Jm_J; kq\rangle \\
&= (-1)^{2k}\delta_{S'S}\sum_{\substack{m_J q\\ m_L' m_S' m_L m_S}}\langle J'm_J' \mid L'm_L'; S'm_S'\rangle\langle Lm_L; Sm_S \mid Jm_J\rangle\langle J'm_J' \mid Jm_J; kq\rangle \\
&\qquad \times\langle L'm_L'|\widetilde{\widetilde{\widetilde{T_q^{(k)}}}}|Lm_L\rangle\delta_{m_{S'}m_S} \\
&= (-1)^{2k}\delta_{S'S}\sum_{\substack{m_J q\\ m_L' m_S' m_L m_S}}\langle J'm_J' \mid L'm_L'; S'm_S'\rangle\langle Lm_L; S'm_S' \mid Jm_J\rangle\langle J'm_J' \mid Jm_J; kq\rangle \\
&\qquad \times\langle L'm_L'|\widetilde{\widetilde{\widetilde{T_q^{(k)}}}}|Lm_L\rangle
\end{aligned} \tag{1.27}$$

In Eq. 1.27 we executed this change of basis and used the known behaviour of $\widetilde{\widetilde{T_q^{(k)}}}$, which is completely analogous to Eq. 1.21. In the following we will exploit the symmetry of Clebsch-Gordan coefficients, that is valid for any angular momentum operator, that satisfies $\hat{\mathbf{J}}_1 + \hat{\mathbf{J}}_2 = \hat{\mathbf{J}}_3$:

$$\langle J_1 m_1; J_2 m_2 \mid J_3 m_3 \rangle = (-1)^{J_1+J_2-J_3} \langle J_2 m_2; J_1 m_1 \mid J_3 m_3 \rangle \tag{1.28}$$

Now we can apply the Wigner-Eckart theorem:

$$\begin{aligned}
\langle J' \| \widetilde{\widetilde{\mathbf{T}_q^{(k)}}} \| J \rangle &= (-1)^{2k} \delta_{S'S} \sum_{\substack{m_J q \\ m'_L m'_S m_L m_S}} \langle J' m'_J \mid L' m'_L; S' m'_S \rangle \langle L m_L; S' m'_S \mid J m_J \rangle \langle J' m'_J \mid J m_J; kq \rangle \\
&\qquad\qquad\qquad \times (-1)^{2k} \langle L' \| \widetilde{\widetilde{\mathbf{T}_q^{(k)}}} \| L \rangle \langle L' m'_L \mid L m_L; kq \rangle \\
&= \delta_{S'S} \sum_{\substack{m_J q \\ m'_L m'_S m_L m_S}} \langle L' m'_L; S' m'_S \mid J' m'_J \rangle \langle L m_L; S' m'_S \mid J m_J \rangle \\
&\qquad\qquad\qquad \times \langle J m_J; kq \mid J' m'_J \rangle \langle L m_L; kq \mid L' m'_L \rangle \langle L' \| \widetilde{\widetilde{\mathbf{T}_q^{(k)}}} \| L \rangle \\
&= \delta_{S'S} \sum_{\substack{m_J q \\ m'_L m'_S m_L m_S}} \langle L' m'_L; S' m'_S | J' m'_J \rangle \langle L m_L; S' m'_S \mid J m_J \rangle \\
&\quad \times (-1)^{J+k-J'} (-1)^{L+k-L'} \langle kq; J m_J \mid J' m'_J \rangle \langle kq; L m_L \mid L' m'_L \rangle \langle L' \| \widetilde{\widetilde{\mathbf{T}_q^{(k)}}} \| L \rangle
\end{aligned} \tag{1.29}$$

Clebsch-Gordon coefficients are closely related to the Wigner symbols [17], as both describe the coupling of angular momenta. We are especially interested in the Wigner $6j$ symbol, which describes the coupling of three momenta, here according to $\hat{\mathbf{J}}_1 + \hat{\mathbf{J}}_2 + \hat{\mathbf{J}}_3 = \hat{\mathbf{J}}$ with further coupling between $\hat{\mathbf{J}}_1 + \hat{\mathbf{J}}_2 = \hat{\mathbf{J}}_{12}$ and $\hat{\mathbf{J}}_2 + \hat{\mathbf{J}}_3 = \hat{\mathbf{J}}_{23}$ (other combinations are possible too). The $6j$ symbol is thus defined by:

$$\begin{Bmatrix} J_1 & J_2 & J_{12} \\ J_3 & J & J_{23} \end{Bmatrix} \equiv \frac{(-1)^{J_1+J_2+J_3+J}}{\sqrt{(2J_{12}+1)(2J_{23}+1)}} \sum_{m_1 m_2 m_3 m_{12} m_{23}} \langle J_{12} m_{12}; J_3 m_3 \mid J m \rangle \tag{1.30}$$

$$\times \langle J_1 m_1; J_2 m_2 \mid J_{12} m_{12} \rangle \langle J_1 m_1; J_{23} m_{23} \mid J m \rangle \langle J_2 m_2; J_3 m_3 \mid J_{23} m_{23} \rangle \tag{1.31}$$

The Wigner $6j$ symbol obeys the following symmetries:

$$\begin{Bmatrix} J_1 & J_2 & J_3 \\ L_1 & L_2 & L_3 \end{Bmatrix} = \begin{Bmatrix} J_2 & J_1 & J_3 \\ L_2 & L_1 & L_3 \end{Bmatrix} = \begin{Bmatrix} J_3 & J_2 & J_1 \\ L_3 & L_2 & L_1 \end{Bmatrix} = \begin{Bmatrix} J_1 & J_3 & J_2 \\ L_1 & L_3 & L_2 \end{Bmatrix} \tag{1.32}$$

Eq. 1.33 displays the invariance under permutations in the columns, whereas Eq. 1.33 showcases the flipping of two elements in one column with respect to their row:

$$\begin{Bmatrix} J_1 & J_2 & J_3 \\ L_1 & L_2 & L_3 \end{Bmatrix} = \begin{Bmatrix} L_1 & L_2 & J_3 \\ J_1 & J_2 & L_3 \end{Bmatrix} = \begin{Bmatrix} L_1 & J_2 & L_3 \\ J_1 & L_2 & J_3 \end{Bmatrix} = \begin{Bmatrix} J_1 & L_2 & L_3 \\ L_1 & J_2 & J_3 \end{Bmatrix} \tag{1.33}$$

This we can use to rewrite the last expression of Eq. 1.29 into a $6j$ symbol, where we set $(\{J, J_1, J_2, J_3, J_{12}, J_{23}\}) \leftrightarrow (\{J', k, L, S', L', J\})$ and use the symmetry relations to obtain:

$$\begin{aligned}
\langle J' \| \widetilde{\widetilde{\widetilde{\mathbf{T}_q^{(k)}}}} \| J \rangle &= \delta_{S'S}(-1)^{J+k-J'}(-1)^{L+k-L'}(-1)^{-k-L-S'-J'}\sqrt{(2L'+1)(2J+1)} \\
&\quad \left\{ \begin{array}{ccc} k & L & L' \\ S' & J' & J \end{array} \right\} \langle L' \| \widetilde{\widetilde{\widetilde{\mathbf{T}_q^{(k)}}}} \| L \rangle \\
&= \delta_{S'S}(-1)^{J-L'+k-S'-2J'}\sqrt{(2J+1)(2L'+1)} \left\{ \begin{array}{ccc} L' & L & k \\ J & J' & S' \end{array} \right\} \langle L' \| \widetilde{\widetilde{\widetilde{\mathbf{T}_q^{(k)}}}} \| L \rangle
\end{aligned} \tag{1.34}$$

where we also used the fact, that $L + S + J \in \mathbb{Z}$ is an integer. By using the action of the operator on one component, we now have arrived at the irreducible matrix element, that can be embedded into Eq. 1.26:

$$\begin{aligned}
\langle \Psi' | \widetilde{T_q^{(k)}} | \Psi \rangle = \sum_{b=1}^{\#\mathcal{B}'} \sum_{p=1}^{\#\mathcal{B}} \mathcal{C}_b'^{*} \mathcal{C}_p (-1)^{-2k} \big(\delta_{S_b' S_p} (-1)^{J_p + L_b' + k + S_b'} \sqrt{(2J_p+1)(2L_b'+1)} \\
\cdot \left\{ \begin{array}{ccc} L_b' & L_p & k_b' \\ J_p & J_b' & S_b' \end{array} \right\} \langle L' || T^{(k)} || L \rangle \big) \langle J'^b m_j{}'^b | J^p m_j{}^p ; k' q' \rangle \, \delta_{I_b' I_p} \, \delta_{m_i'^b m_i^p})
\end{aligned} \tag{1.35}$$

Finally we can identify $\widetilde{T_q^{(k)}}$ with dipole operator $\hat{d}_q$, which is a rank one operator, such that $k = 1$. Since there are for the Potassium atom 16 eigenstates for the excited state of the $D2$-line and 8 for the corresponding ground state, the sum in Eq. 1.35 can have up to 128 constituents. However not all contributions are equally significant, wherefore this sum reduces considerably when we filter minor weighing factors. The latter can be found by diagonalising the Hamiltonian and extracting the eigenvectors as discussed in Sec. 1.3.2. The eigenvectors deliver the factors $\mathcal{C}_b'(B)$ and $\mathcal{C}_p(B)$ needed to change into the eigenbasis of the system at a given magnetic field strength. We will emphasize at this point, that this implies, that the number of significant terms in Eq. 1.35 depends on the strength of the applied magnetic field.

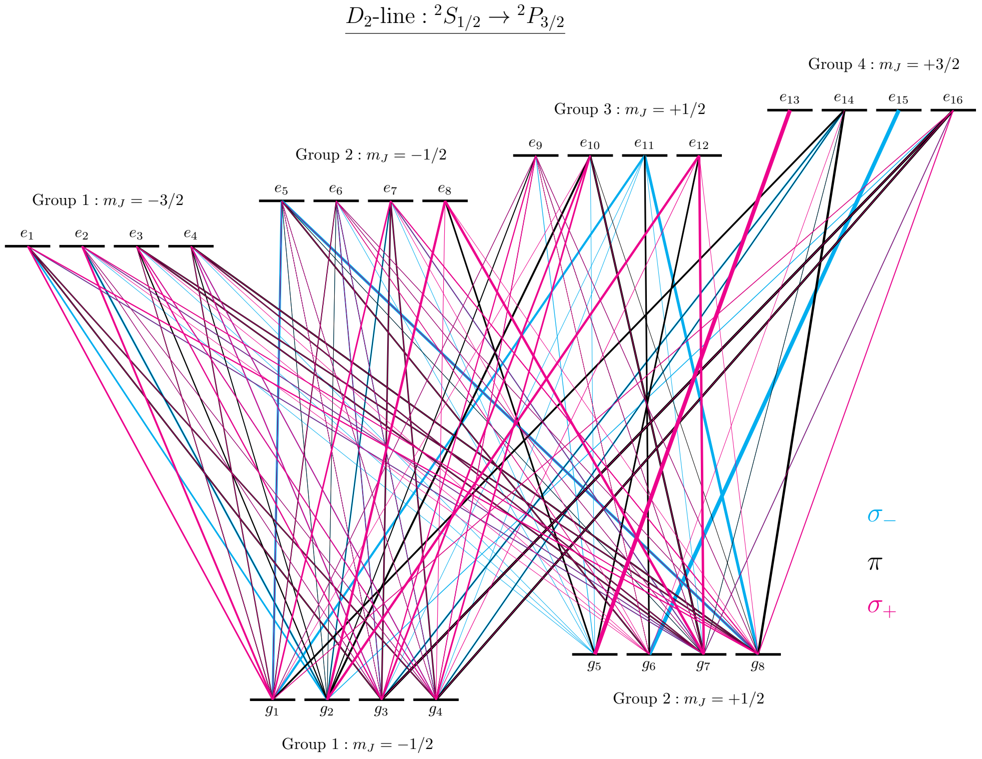

(a) *Dipole matrix elements for* $B = 0\,G$

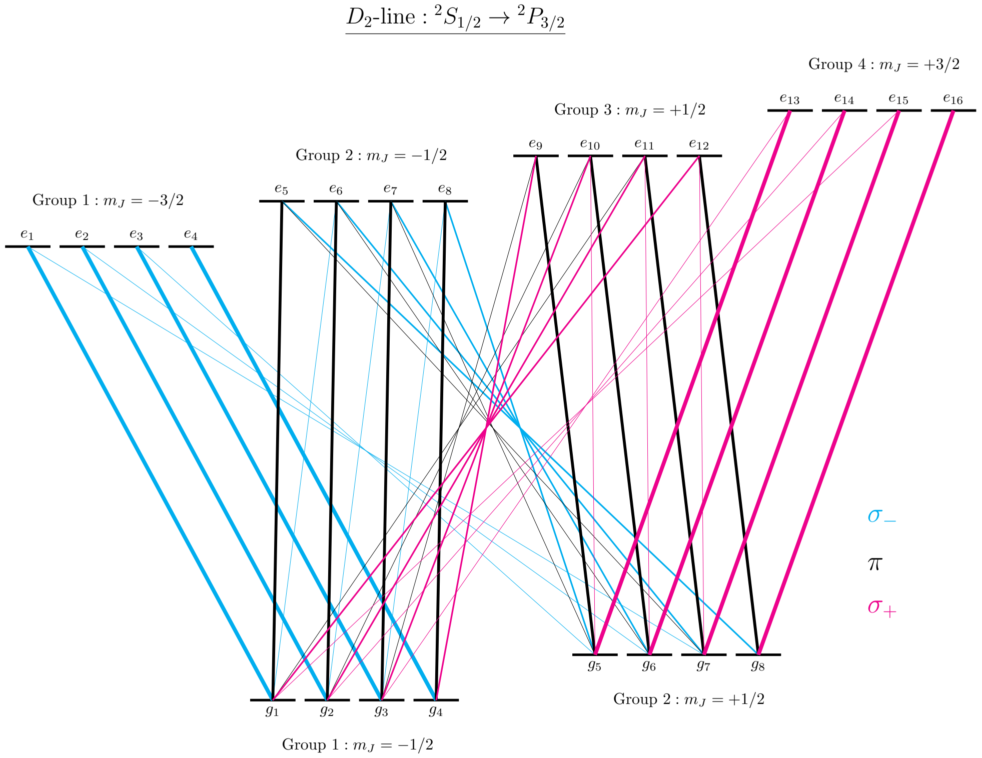

(b) *Dipole matrix elements for* $B = 562\,G$

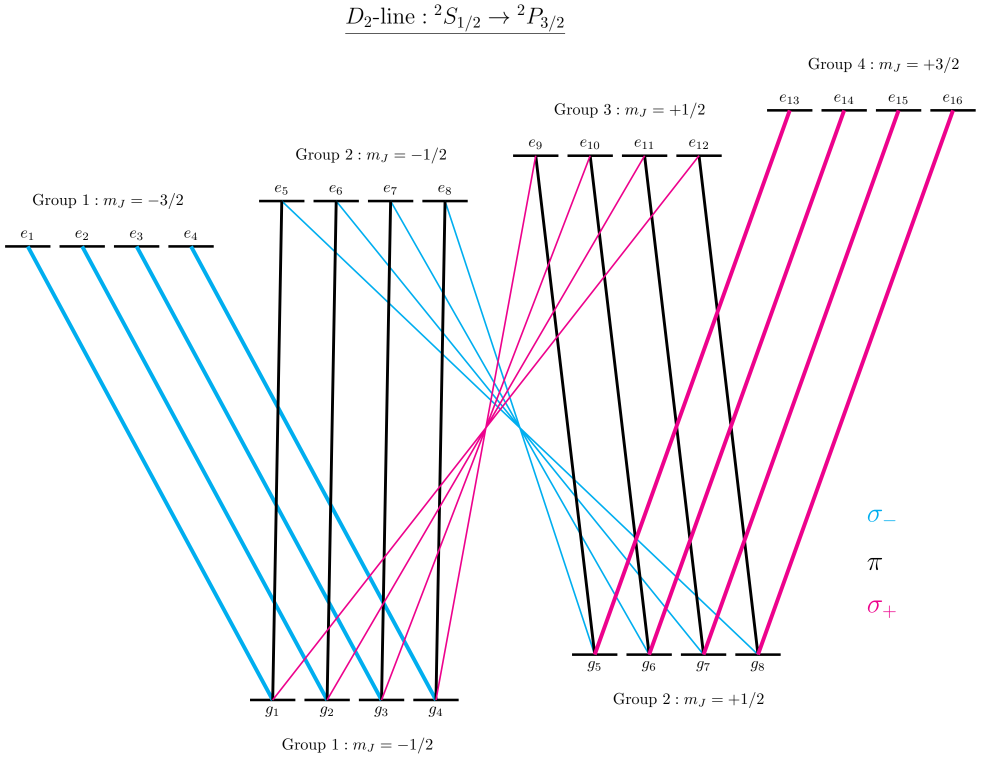

(**c**) *Dipole matrix elements for* $B = 7000\,G$

Figure 1.4: ***Dipole matrix elements of*** D_2***-line.*** *Dipole transitions for various magnetic fields shown in the eigenbasis of the Hamiltonian. Groups consist of eigenstates with predominant* m_J *contribution. Transition strengths are portrayed logarithmic in width and transitions with a decay probabilities smaller than* 10^{-6} *are neglected. The first subfigure* (**a**) *is at zero field in the Basis as described in Eq. 1.16. It can be seen, that here this is an unfavorable basis choice. In proximity to the Feshbach resonance at* $B = 562\,G$ *the decay structure* (**b**) *reduces considerably. In the high field limit* (**c**) *the used basis vectors have only one dominant contribution from the respective* I, J*-state.*

In Fig. 1.4 we used Eq. 1.35 to calculate the dipole matrix elements for the D_2-line of ${}^{39}K$. We portrayed three scenarios, which are zero magnetic field, intermediate and strong magnetic fields. We can see that for no field the I, J-basis is a bad choice and results in plenty of decay modes, which can better be described using the F, m_F-basis. For intermediate magnetic field, the I, J-basis produces the additional decay modes, that cause dark state formations. We chose a magnetic field strength of $B = 562G$ because the Feshbach resonance, that we exploit in the experiment is located here. For the high field regime the additional decay modes disappear and the I, J-basis can be approximated as being pure.

1.5 Atom Photon Interaction

In this section we want to give an overview on the interaction between photons and potassium atoms, that occur during the imaging process and thus are of key importance to us. To this end it is instructive for the reader to first understand the dynamics in a two level atom and then generalise for the multilevel structure that is inherent to potassium atoms (shown in Fig. 1.5) as used in the experiment. Here we will directly start with the multilevel structure, since we are not interested in the two level atom. The system consists of energy eigenstates $|i\rangle$ with energy E_i. Therefore the corresponding Hilbert space is spanned by the basis $\mathcal{B} = \{|i\rangle\}$ with $i \in 1, ..., N$. We may thus construct the atomic Hamiltonian as:

$$\hat{\mathcal{H}}_0 = \sum_{i=1}^{N} \hbar\omega_i |i\rangle\langle i| \ , \quad |i\rangle \in \mathcal{B} \tag{1.36}$$

The complete Hamiltonian can be derived from considerations on the nature of the interaction. To this end we will treat the incident light beam as classical electric field, rather than quantised excitations of the electromagnetic field in QED, as one my initially expect in the frame work of quantum optics, however the classical treatment is sufficient. For now the interaction Hamiltonian in dipole approximation is [16]:

$$\mathcal{H}' = -\mathbf{d} \cdot \mathbf{E} \tag{1.37}$$

Here $\mathbf{d} = -e \cdot \mathbf{r}$ is the dipole operator and $\mathbf{E}$ is electric field operator. We can use the parity operator Π to specify Eq. 1.37, which is defined by the action upon the position operator $\mathbf{r}$ with $\Pi\mathbf{r}\Pi^\dagger = -\mathbf{r}$. Therefore we can write for the anticommutator: $\{\Pi, \mathbf{r}\} = 0$, which leads us to conclude that:

$$\langle i|\{\Pi, \mathbf{r}\}|j\rangle = 0 \tag{1.38}$$

This argument obviously requires the atomic states to be parity eigenstates. However we can assume this, because the inner orbital angular momenta sum to zero, such that we can treat the atom as a central force problem, which in return is the case for the hydrogen atom, that has energyeigenfunctions, which are parity eigenstates. This true since the angular momentum part of the hydrogen eigenstates, the spherical harmonics Y_{lm}, are parity eigenstates and transform identically under action of the parity operator: $\Pi\, Y_{lm} = Y_{lm}(\pi - \vartheta, \pi + \varphi) = (-1)^l \cdot Y_{lm}(\vartheta, \varphi)$ as required for our argument. Since $\Pi^2 = 1$ and is a unitary transformation, we can deduce that:

$$\langle i|\{\Pi, \mathbf{r}\}|j\rangle = \langle i|\Pi\mathbf{r} + \mathbf{r}\Pi|j\rangle = (\pi_i + \pi_j)\langle i|\mathbf{r}|j\rangle \tag{1.39}$$

with π_i, π_j being the eigenvalues of Π. By recalling that $\Pi^2 = 1$ we can conclude that all possible eigenvalues are ± 1, that correspond to even and odd parity respectively, and thus, that either $(\pi_i + \pi_j) = 0$ or $\langle i|\mathbf{r}|j\rangle = 0$. Because π_i, π_j are nonzero, we know that for the dipole operator, which is proportional to $\mathbf{r}$, only opposite parity eigenstates are coupled by

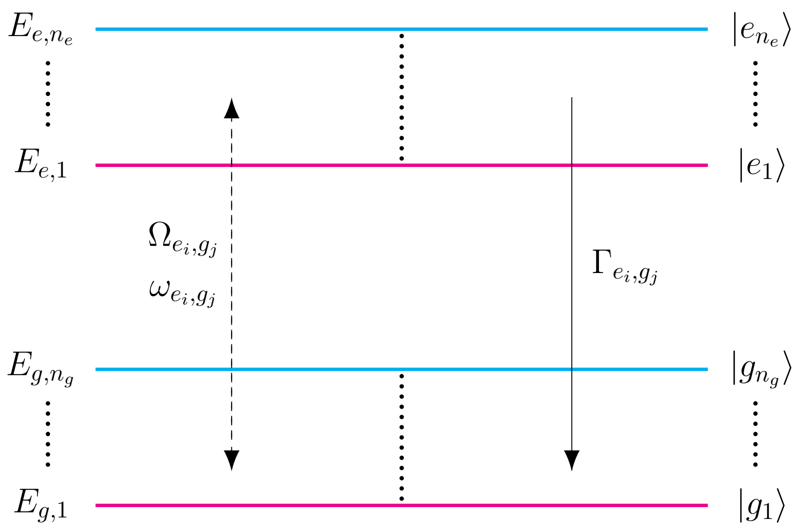

Figure 1.5: ***Atomic multilevel structure.*** *Excited levels are coupled to ground states via decays with rate Γ_{e_i,g_j}, frequency ω_{e_i,g_j} and Rabi-frequency Ω_{e_i,g_j}.*

the Hamiltonian. Now the electric field is treated, as previously mentioned, classically:

$$\vec{E}(\vec{r},t) = E_0\,\vec{\epsilon}\,\cos\Big(\vec{k}\cdot\vec{r} - \omega\cdot t\Big) \tag{1.40}$$

With this form for the electric field we obtain for all energy levels:

$$\begin{aligned}\mathcal{H}' &= -\sum_{i\neq j} eE_0\cos\left(\vec{k}\cdot\vec{r}-\omega_l t\right)\langle i|\hat{\vec{\epsilon}}\cdot\hat{\vec{r}}|j\rangle|i\rangle\langle j| \qquad (1.41)\\ &= \frac{\hbar}{2}\sum_{i\neq j}\cos\Big(\vec{k}\cdot\vec{r}-\omega_l t\Big)\left(\Omega_{ij}|i\rangle\langle j| + \Omega^*_{ij}|j\rangle\langle i|\right) \qquad (1.42)\end{aligned}$$

Where we have just defined the Rabi frequency Ω as:

$$\Omega_{ij} = -\frac{E_0}{\hbar}\langle i|\hat{\vec{\epsilon}}\cdot\hat{\vec{d}}|j\rangle \tag{1.43}$$

The summation in Eq. 1.42 reflects our conclusions on the contributing matrix elements, such that $i, j \in \{1, \dots, n_{e,g}\}$ respectively:

$$\hat{\mathcal{H}}' = \sum_{i=1}^{n_e}\sum_{j=n_e+1}^{N}\hbar\cos\left(-\omega_l t\right)\left(\Omega_{ij}|i\rangle\left\langle j\right| + \Omega^*_{ij}\left| j\right\rangle\langle i|\right) \tag{1.44}$$

By now boosting into the interaction frame, which is to say that we transform $\mathcal{H}'$ according to:

$$\hat{\mathcal{H}}_I = \exp\left(\frac{i}{\hbar}\hat{\mathcal{H}}_0 t\right)\hat{\mathcal{H}}'\exp\left(-\frac{i}{\hbar}\hat{\mathcal{H}}_0 t\right) \tag{1.45}$$

we obtain our final formula for the Hamiltonian, while also using the so-called rotating wave approximation (RWA). In the approximation we seek a form, that decomposes the cosine in Eq. 1.44 into a positive and negative rotation, i.e. the exponential function. By discarding fast oscillations, we can simplify our formulae significantly. The calculations follow closely to [18] and are presented here:

$$\begin{aligned}
\hat{\mathcal{H}}_I &= \sum_{n=1}^{N} e^{i\omega_n t}|n\rangle\langle n| \sum_{i=1}^{n_e} \sum_{j=n_e+1}^{N} \hbar\cos(-\omega_l t)(\Omega_{ij}|i\rangle\langle j| + \Omega_{ij}^{*}|j\rangle\langle i|) \sum_{m=1}^{N} e^{-i\omega_m t}|m\rangle\langle m| \\
&= \sum_{n,m=1}^{N} \sum_{i=1}^{n_e} \sum_{j=n_e+1}^{N} e^{i(\omega_n-\omega_m)t}\hbar\cos(-\omega_l t)[\Omega_{ij}|n\rangle\langle n \mid i\rangle\langle j \mid m\rangle\langle m| + \Omega_{ij}^{*}|n\rangle\langle n \mid j\rangle\langle i \mid m\rangle\langle m|] \\
&= \sum_{n,m=1}^{N} \sum_{i=1}^{n_e} \sum_{j=n_e+1}^{N} e^{i(\omega_n-\omega_m)t}\hbar\cos(-\omega_l t)[\Omega_{ij}\delta_{ni}\delta_{jm}|n\rangle\langle m| + \Omega_{ij}^{*}\delta_{nj}\delta_{im}|n\rangle\langle m|] \\
&= \sum_{i=1}^{n_e} \sum_{j=n_e+1}^{N} \hbar\cos(-\omega_l t)[\Omega_{ij}e^{i\omega_{ij}t}|i\rangle\langle j| + \Omega_{ij}^{*}e^{-i\omega_{ij}t}|j\rangle\langle i|] \\
&\approx \sum_{i=1}^{n_e} \sum_{j=n_e+1}^{N} \frac{\hbar}{2}[\Omega_{ij}e^{-i\delta_{ij}t}|i\rangle\langle j| + \Omega_{ij}^{*}e^{i\delta_{ij}t}|j\rangle\langle i|]
\end{aligned} \tag{1.46}$$

1.6 Lindblad Master Equation

In this section we will look closer at the concept of master equations and motivate the use of the Lindbladian to describe our system. Since we are interested in the time evolution of the imaging process we must investigate the states that the atoms will have. Usually in quantum dynamics, one would now take the initial state of the system and evolve it with a unitary time evolution according to the Schrödinger equation. However the unitary dynamics do not account for processes like decays and thus require a constant phase coherence. Therefore we need a different approach, which is the evolution of the density matrix by non-unitary time evolution operators. This step is crucial to analyse the system since spontaneous decays and coherences are of central interest. By allowing interactions between the system and its environment we effectively model an open quantum system.

We will however remain in the field of classical quantum dynamics and only include QED effects in an effective approach, where we introduce them as phenomenological terms as Linblad superoperator. We already discussed the interaction between the atoms and photons in section 1.5 and therefore can simply define the Lindblad equation as [19]:

$$\frac{d\hat{\rho}}{dt} = -\frac{i}{\hbar}\left[\hat{\mathcal{H}}_I, \hat{\rho}\right] + \mathcal{L}_{\text{phen}}(\hat{\rho}) \tag{1.47}$$

The brackets in Eq. 1.47 represent the commutator and without the phenomenological term, the Lindbladian is equivalent to the von-Neumann equation. The density matrix is:

$$\hat{\rho} = \sum_k p_k \left|\psi_k\right\rangle \left\langle\psi_k\right| \tag{1.48}$$

where p_k represent the probability to find the system in a pure state $|\psi_k\rangle$. In our case the phenomenological part is given by:

$$\begin{aligned} \mathcal{L}_{\text{phen}}\left(\hat{\rho}\right) &= \mathcal{D}[\hat{c}]\hat{\rho} \\ \mathcal{D}[\hat{c}]\hat{\rho} &= \hat{c}\hat{\rho}\hat{c}^\dagger - \frac{1}{2}\left(\hat{c}^\dagger\hat{c}\hat{\rho} + \hat{\rho}\hat{c}^\dagger\hat{c}\right) \end{aligned} \tag{1.49}$$

Here $\mathcal{D}[\hat{c}]\hat{\rho}$ is the so-called superoperator and $\hat{c}$ is the collapse operator:

$$\hat{c}_{|e_i\rangle\rightarrow|g_j\rangle} = \left|g_j\right\rangle\left\langle e_i\right|\sqrt{\Gamma_{|e_i\rangle\rightarrow|g_j\rangle}} \tag{1.50}$$

The rate with which this decay channel occurs is defined by Γ. With Eq. 1.47 we can now access the populations and coherences of the system. It should be mentioned, that the Lindblad equation only describes a single atom and its evolution, but does not describe the entire ensemble of atoms in the BEC.

1.6.1 Maxwell-Bloch Equations

From the Lindblad equation we will now derive the Maxwell-Bloch equations, which typically describe the dynamics of a two level system, we must however expand to the four level structure, because it will be used for the proposed imaging scheme. The resulting differential equations represent the evolution of the mean populations and coherences. The density operator $\hat{\rho}$ can represented in this approximation by the 4×4 matrix:

$$\hat{\rho} = \begin{pmatrix} \rho_{e_1e_1} & \rho_{e_1e_2} & \rho_{e_1g_1} & \rho_{e_1g_2} \\ \rho_{e_2e_1} & \rho_{e_2e_2} & \rho_{e_2g_1} & \rho_{e_2g_2} \\ \rho_{g_1e_1} & \rho_{g_1e_2} & \rho_{g_1g_1} & \rho_{g_1g_2} \\ \rho_{g_2e_1} & \rho_{g_2e_2} & \rho_{g_2g_1} & \rho_{g_2g_2} \end{pmatrix} \tag{1.51}$$

The Hamiltonian can be calculated from Eq. 1.46. For imaging purposes we are only interested in shining two light frequencies on the atomic sample, such that only two different Rabi frequencies will appear:

$$\hat{\mathcal{H}}_I = \frac{\hbar}{2}\begin{pmatrix} 0 & 0 & \Omega_{e_1g_1}e^{-i\delta_{e_1g_1}t} & 0 \\ 0 & 0 & 0 & \Omega_{e_2g_2}e^{-i\delta_{e_2g_2}t} \\ \Omega^*_{e_1g_1}e^{+i\delta_{e_1g_1}t} & 0 & 0 & 0 \\ 0 & \Omega^*_{e_2g_2}e^{+i\delta_{e_2g_2}t} & 0 & 0 \end{pmatrix} \tag{1.52}$$

From the calculations of Sec. 1.4 we know, that there are four main decay modes, that need to be considered:

$$\begin{aligned} \hat{c}_{|e_1\rangle\to|g_1\rangle} &= |g_1\rangle\langle e_1|\sqrt{\Gamma_{|e_1\rangle\to|g_1\rangle}}, & \hat{c}_{|e_2\rangle\to|g_1\rangle} &= |g_1\rangle\langle e_2|\sqrt{\Gamma_{|e_2\rangle\to|g_1\rangle}} \\ \hat{c}_{|e_1\rangle\to|g_2\rangle} &= |g_2\rangle\langle e_1|\sqrt{\Gamma_{|e_1\rangle\to|g_2\rangle}}, & \hat{c}_{|e_2\rangle\to|g_2\rangle} &= |g_2\rangle\langle e_2|\sqrt{\Gamma_{|e_2\rangle\to|g_2\rangle}} \end{aligned} \tag{1.53}$$

Together with the collapse operators, we are able to calculate all entries of Eq. 1.47. The resulting Maxwell-Bloch Equations contain information on the coherences which are the non-diagonal elements of the $\hat{\rho}$. The diagonal elements are the populations of each energy eigenstate of the system. The reader should be reminded, that the size of the density matrix scales with N^2, wherefore we have a system of sixteen coupled differential equation:

$$\begin{aligned}
\dot{\rho}_{e1e1} &= -\Gamma_{e_1g_1}\rho_{e_1e_1} - \Gamma_{e_1g_2}\rho_{e_1e_1} - \tfrac{i}{2}\left(-\rho_{e_1g_1}\Omega^*_{e_1g_1}e^{+i\delta_{e_1g_1}t} + \rho_{g_1e_1}\Omega_{e_1g_1}e^{-i\delta_{e_1g_1}t}\right) \\
\dot{\rho}_{e1e2} &= -\tfrac{1}{2}\Gamma_{e_1g_1}\rho_{e_1e_2} - \tfrac{1}{2}\Gamma_{e_1g_2}\rho_{e_1e_2} - \tfrac{1}{2}\Gamma_{e_2g_1}\rho_{e_1e_2} - \tfrac{1}{2}\Gamma_{e_2g_2}\rho_{e_1e_2} \\
&\qquad -\tfrac{i}{2}\left(-\rho_{e_1g_2}\Omega^*_{e_2g_2}e^{+i\delta_{e_2g_2}t} + \rho_{g_1e_2}\Omega_{e_1g_1}e^{-i\delta_{e_1g_1}t}\right) \\
\dot{\rho}_{e1g1} &= -\tfrac{1}{2}\Gamma_{e_1g_1}\rho_{e_1g_1} - \tfrac{1}{2}\Gamma_{e_1g_2}\rho_{e_1g_1} - \tfrac{i}{2}\left(-\rho_{e_1e_1}\Omega_{e_1g_1}e^{-i\delta_{e_1g_1}t} + \rho_{g_1g_1}\Omega_{e_1g_1}e^{-i\delta_{e_1g_1}t}\right) \\
\dot{\rho}_{e1g2} &= -\tfrac{1}{2}\Gamma_{e_1g_1}\rho_{e_1g_2} - \tfrac{1}{2}\Gamma_{e_1g_2}\rho_{e_1g_2} - \tfrac{i}{2}\left(-\rho_{e_1e_2}\Omega_{e_2g_2}e^{-i\delta_{e_2g_2}t} + \rho_{g_1g_2}\Omega_{e_1g_1}e^{-i\delta_{e_1g_1}t}\right) \\
\dot{\rho}_{e2e1} &= -\tfrac{1}{2}\Gamma_{e_1g_1}\rho_{e_2e_1} - \tfrac{1}{2}\Gamma_{e_1g_2}\rho_{e_2e_1} - \tfrac{1}{2}\Gamma_{e_2g_1}\rho_{e_2e_1} - \tfrac{1}{2}\Gamma_{e_2g_2}\rho_{e_2e_1} \\
&\qquad -\tfrac{i}{2}\left(-\rho_{e_2g_1}\Omega^*_{e_1g_1}e^{+i\delta_{e_1g_1}t} + \rho_{g_2e_1}\Omega_{e_2g_2}e^{-i\delta_{e_2g_2}t}\right) \\
\dot{\rho}_{e2e2} &= -\Gamma_{e_2g_1}\rho_{e_2e_2} - \Gamma_{e_2g_2}\rho_{e_2e_2} - \tfrac{i}{2}\left(-\rho_{e_2g_2}\Omega^*_{e_2g_2}e^{+i\delta_{e_2g_2}t} + \rho_{g_2e_2}\Omega_{e_2g_2}e^{-i\delta_{e_2g_2}t}\right) \\
\dot{\rho}_{e2g1} &= -\tfrac{1}{2}\Gamma_{e_2g_1}\rho_{e_2g_1} - \tfrac{1}{2}\Gamma_{e_2g_2}\rho_{e_2g_1} - \tfrac{i}{2}\left(-\rho_{e_2e_1}\Omega_{e_1g_1}e^{-i\delta_{e_1g_1}t} + \rho_{g_2g_1}\Omega_{e_2g_2}e^{-i\delta_{e_2g_2}t}\right) \\
\dot{\rho}_{e2g2} &= -\tfrac{1}{2}\Gamma_{e_2g_1}\rho_{e_2g_2} - \tfrac{1}{2}\Gamma_{e_2g_2}\rho_{e_2g_2} - \tfrac{i}{2}\left(-\rho_{e_2e_2}\Omega_{e_2g_2}e^{-i\delta_{e_2g_2}t} + \rho_{g_2g_2}\Omega_{e_2g_2}e^{-i\delta_{e_2g_2}t}\right) \\
\dot{\rho}_{g1e1} &= -\tfrac{1}{2}\Gamma_{e_1g_1}\rho_{g_1e_1} - \tfrac{1}{2}\Gamma_{e_1g_2}\rho_{g_1e_1} - \tfrac{i}{2}\left(\rho_{e_1e_1}\Omega^*_{e_1g_1}e^{+i\delta_{e_1g_1}t} - \rho_{g_1g_1}\Omega^*_{e_1g_1}e^{+i\delta_{e_1g_1}t}\right) \\
\dot{\rho}_{g1e2} &= -\tfrac{1}{2}\Gamma_{e_2g_1}\rho_{g_1e_2} - \tfrac{1}{2}\Gamma_{e_2g_2}\rho_{g_1e_2} - \tfrac{i}{2}\left(\rho_{e_1e_2}\Omega^*_{e_1g_1}e^{+i\delta_{e_1g_1}t} - \rho_{g_1g_2}\Omega^*_{e_2g_2}e^{+i\delta_{e_2g_2}t}\right) \\
\dot{\rho}_{g1g1} &= \Gamma_{e_1g_1}\rho_{e_1e_1} + \Gamma_{e_2g_1}\rho_{e_2e_2} - \tfrac{i}{2}\left(\rho_{e_1g_1}\Omega^*_{e_1g_1}e^{+i\delta_{e_1g_1}t} - \rho_{g_1e_1}\Omega_{e_1g_1}e^{-i\delta_{e_1g_1}t}\right) \\
\dot{\rho}_{g1g2} &= -\tfrac{i}{2}\left(\rho_{e_1g_2}\Omega^*_{e_ig_1}e^{+i\delta_{e_1g_1}t} - \rho_{g_1e_2}\Omega_{e_2g_2}e^{-i\delta_{e_2g_2}t}\right) \\
\dot{\rho}_{g2e1} &= -\tfrac{1}{2}\Gamma_{e_1g_1}\rho_{g_2e_1} - \tfrac{1}{2}\Gamma_{e_1g_2}\rho_{g_2e_1} - \tfrac{i}{2}\left(\rho_{e_2e_1}\Omega^*_{e_2g_2}e^{+i\delta_{e_2g_2}t} - \rho_{g_2g_1}\Omega^*_{e_1g_1}e^{+i\delta_{e_1g_1}t}\right) \\
\dot{\rho}_{g2e2} &= -\tfrac{1}{2}\Gamma_{e_2g_1}\rho_{g_2e_2} - \tfrac{1}{2}\Gamma_{e_2g_2}\rho_{g_2e_2} - \tfrac{i}{2}\left(\rho_{e_2e_2}\Omega^*_{e_2g_2}e^{+i\delta_{e_2g_2}t} - \rho_{g_2g_2}\Omega^*_{e_2g_2}e^{+i\delta_{e_2g_2}t}\right) \\
\dot{\rho}_{g2g1} &= -\tfrac{i}{2}\left(\rho_{e_2g_1}\Omega^*_{e_2g_2}e^{+i\delta_{e_2g_2}t} - \rho_{g_2e_1}\Omega_{e_1g_1}e^{-i\delta_{e_1g_1}t}\right) \\
\dot{\rho}_{g2g2} &= \Gamma_{e_1g_2}\rho_{e_ee_1} + \Gamma_{e_2g_2}\rho_{e_2e_2} - \tfrac{i}{2}\left(\rho_{e_2g_2}\Omega^*_{e_2g_2}e^{+i\delta_{e_2g_2}t} - \rho_{g_2e_2}\Omega_{e_2g_2}e^{-i\delta_{e_2g_2}t}\right)
\end{aligned} \tag{1.54}$$

1.6.2 Scattering Cross Section

From the optical Bloch equations we can derive properties of the system such as the scattering cross section σ and the saturation intensity I_{sat}. For both parameters will prove important to the description of the imaging technique in Sec. 1.7. The following calculations are only valid in the steady state scenario and are oriented on [16]. If one wanted to obtain the correct values, the coupled differential equations would have to be solved numerically. We may start the derivation of the scattering cross section by making simplifications to our formulae in Eq. 1.54. In pursuit of generality we will exploit the symmetry of our level structure and define for now $\dot{\rho}_{e_1e_1} = \dot{\rho}_{e2e2} = \dot{\rho}_{ee}$ and $\Gamma_{e_1g_1} + \Gamma_{e_1g_2} = \Gamma_{e_2g_1} + \Gamma_{e_2g_2} = \Gamma$ and proceed analogously for the coherences, δ and Ω. An important note to make here is, that we have just reduced each branch in our four level system into an effective two level system, which is only possible because of the before mentioned symmetry. Since an appropriate measure for scattering is given by the populations in the excited state, we are interested in the behaviour of $\dot{\rho}_{ee}$, which in general terms for both $\dot{\rho}_{e_1e_1} = \dot{\rho}_{e2e2}$ is defined by:

$$\dot{\rho}_{ee} = -\Gamma\rho_{ee} + i\frac{\Omega}{2}(\rho_{eg}e^{i\delta t} - \rho_{ge}e^{-i\delta t}) \tag{1.55}$$

The respective coherences are:

$$\dot{\rho}_{eg} = -\frac{\Gamma}{2}\rho_{eg} + i\frac{\Omega}{2}(\rho_{ee}e^{-i\delta t} - \rho_{gg}e^{-i\delta t}) \tag{1.56}$$

$$\dot{\rho}_{ge} = -\frac{\Gamma}{2}\rho_{ge} + i\frac{\Omega}{2}(\rho_{gg}e^{i\delta t} - \rho_{ee}e^{i\delta t}) \tag{1.57}$$

We can boost into the rotating frame of the light by employing the definitions $\bar{\rho}_{ge} \equiv \rho_{ge}e^{-i\delta t}$ and $\bar{\rho}_{eg} \equiv \rho_{eg}e^{i\delta t}$ and obtain:

$$\dot{\bar{\rho}}_{eg} = -(\frac{\Gamma}{2} - i\delta)\bar{\rho}_{eg} + i\frac{\Omega}{2}(\rho_{ee} - \rho_{gg}) \tag{1.58}$$

$$\dot{\bar{\rho}}_{ge} = -(\frac{\Gamma}{2} + i\delta)\bar{\rho}_{ge} + i\frac{\Omega}{2}(\rho_{gg} - \rho_{ee}) \tag{1.59}$$

If we assume that the coherences settle quickly compared to the evolution of the populations, we can use this decoupling of time scales to motivate an adiabatic approximation resulting in:

$$\left(\frac{\Gamma}{2} - i\delta\right)\bar{\rho}_{\mathrm{eg}} = i\frac{\Omega}{2}\left(\rho_{\mathrm{ee}} - \rho_{\mathrm{gg}}\right) \quad (\text{for } \partial_t\bar{\rho}_{\mathrm{eg}} \approx 0) \tag{1.60}$$

$$\left(\frac{\Gamma}{2} + i\delta\right)\bar{\rho}_{\mathrm{ge}} = -i\frac{\Omega}{2}\left(\rho_{\mathrm{ee}} - \rho_{\mathrm{gg}}\right) \quad (\text{for } \partial_t\bar{\rho}_{\mathrm{ge}} \approx 0) \tag{1.61}$$

By combining these relations we get:

$$\frac{\Gamma}{2}\left(1 + \frac{\delta^2}{\frac{\Gamma}{2}^2}\right)\left(\bar{\rho}_{\mathrm{eg}} - \bar{\rho}_{\mathrm{ge}}\right) = i\Omega\left(\rho_{\mathrm{ee}} - \rho_{\mathrm{gg}}\right) \tag{1.62}$$

which we can insert into the excited state populations function to yield:

$$\partial_t \rho_{\mathrm{ee}} = -\Gamma \rho_{\mathrm{ee}} - \frac{\Omega^2}{2\frac{\Gamma}{2}\left(1 + \delta^2/\frac{\Gamma}{2}^2\right)} \left(\rho_{\mathrm{ee}} - \rho_{\mathrm{gg}}\right) \tag{1.63}$$

We will not derive the complete steady state solution ($\partial_t \rho_{ee} = 0$) here, but only present the result for the two-level system, which was taken from [16]. It should be mentioned, that this is a significant assumption, since we will see in Sec. 2.2 that both imaging branches influence each other. In order to recover this fact, one has to use numerical means (Sec. 2.1).

$$\lim_{t\to\infty} \rho_{ee} = \frac{\Omega^2/\Gamma^2}{1 + \left(\frac{2\delta}{\Gamma}\right)^2 + 2\frac{\Omega^2}{\Gamma^2}} \tag{1.64}$$

From the steady state solution we can define the scattering rate and the total scattered power:

$$R_{sc} = \Gamma \lim_{t\to\infty} \rho_{ee} \quad \text{and} \quad P_{sc} = \hbar\omega_0 \Gamma \lim_{t\to\infty} \rho_{ee} \tag{1.65}$$

From Eq. 1.43 we know that Ω_{ij} is proportional to the light intensity I, thus the definition from the saturation intensity I_{sat} is logical:

$$\frac{I}{I_{\mathrm{sat}}} \equiv \frac{2\Omega^2}{\Gamma^2} \tag{1.66}$$

With this relation we can rewrite the steady state solution for the excited state to:

$$\lim_{t\to\infty} \rho_{ee} = \frac{1}{2} \frac{I/I_{\mathrm{sat}}}{1 + 4\delta^2/\Gamma^2 + I/I_{\mathrm{sat}}} \tag{1.67}$$

This expression can be compared to the radiated power from Eq. 1.65, while also using $P_{\mathrm{sc}} = \sigma_{\mathrm{sc}} I$ in order to obtain the scattering cross section:

$$\sigma_{\mathrm{sc}} = \frac{\sigma_0}{1 + 4\delta^2/\Gamma^2 + I/I_{\mathrm{sat}}}, \tag{1.68}$$

where the resonant cross section $\sigma_0 = \hbar\omega_0\Gamma/2I_{\mathrm{sat}}$ has been defined. The saturation intensity I_{sat} in return can be recovered from Eq. 1.67 by calculating the Rabi frequency and determining the decay rate Γ. For the D_2-line of $^{39}\mathbf{K}$ the saturation intensity is $I_{\mathrm{sat}} = 1.75 mW/cm^2$ [9]. Why and when this reduction to a two-level system is justified, will be shown in Sec. 2.3.

1.7 Absorption Imaging in Multilevel Structure

In the course of this thesis our main target is the description of a *closed* cycle imaging scheme for potassium at intermediate magnetic fields. Here we define the intermediate field regime as the range, in which the excited states are approximately pure m_I and m_J states and the ground states can be mixed. The cooling procedure needed to achieve condensation produces atoms in the ground state $|g_3\rangle$ from Fig. 1.4. Now one could simply lower the magnetic fields before imaging the atoms, but as we have seen in Sec. 1.2 there are several Feshbach resonance obstructing the way to zero magnetic field, which would unintentionally modulate the interaction strength. Therefore we remain at this magnetic field. The four-level system, that appears from considerations in Sec. 1.4, spans between two hyperfine states of the $S_{1/2}$ ground state manifold and two hyperfine states of the $P_{3/2}$ excited state manifold. Usually imaging occurs between the before mentioned ground state $|g_3\rangle$ and the excited state $|e_3\rangle$ using an imaging beam, which is the so-called *cooler*. Now the excited state $|e_3\rangle$ posses two decay modes, one that is dominant with a probability of 98% and decays back into $|g_3\rangle$. The other decay with 2% decays into $|g_5\rangle$, while both decays are σ^--light. This state will populate and thus form a dark state. The typical timescale is very fast ($\sim 2\mu s$ for a loss of half the population into the dark state). To achieve the sought after closed imaging scheme, we use a secondary laser light, the so-called *repumper*, which is σ^+-light. The corresponding excited state in the $P_{3/2}$ manifold is the state $|e_{13}\rangle$, which dominantly decays back to the ground state $|g_5\rangle$, but also weakly to the original ground state $|g_3\rangle$. Thus we have closed imaging scheme. Interestingly, the repumper branch exhibits almost prefect symmetry to the cooler branch, meaning that the decay probabilities are approximately the same.

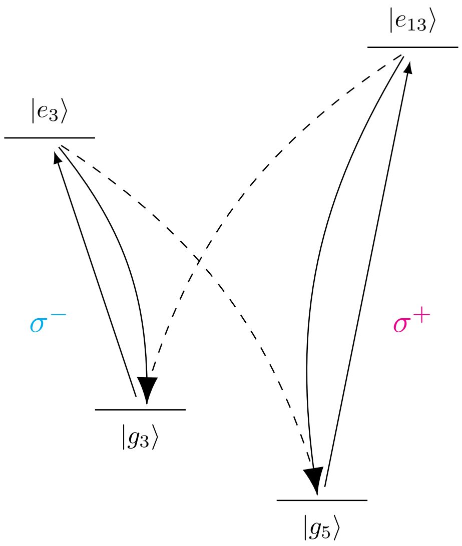

Figure 1.6: ***Closed four level system for imaging.*** *The atomic ground state of our system is $|g_3\rangle$ and the cooler imaging transition (σ^-) transfers atoms the excited state $|e_3\rangle$. Because of the decay from this state the (dark) state $|g_5\rangle$ is populated and atoms are thereby lost from $|e_3\rangle$. To overcome this, a repumper imaging transition (σ^+) is introduced. It couples the state $|g_5\rangle$ to the excited state $|e_{13}\rangle$ from where the atoms can decay back into $|g_3\rangle$ and the system becomes closed.*

Chapter 2

Numerical Results

2.1 Evolution of Multilevel Atom Populations

In order to analyse the temporal evolution of the populations in the multilevel atom, we can solve the Lindblad equation (1.47). Since solutions are far from simple to guess, we employ numerical integrators, that can find solutions for this type of equation. Specifically we define a basis for the multilevel system and use this to construct the Lindblad master equation, which together with a set of appropriate collapse operators forms the Liouvillian superoperator in matrix form. This matrix is projected onto the initial state and integrated with respect to time using *scipy.integrate.ode* [1]. The described process is equivalent to the temporal evolution of the density matrix on a given time grid. In principle one could investigate any multilevel atom in the described manner and make predictions on the interaction with light quanta. Instead we will womanly focus on the four level structure, as described in Sec. 1.7, since it is most important to our understanding of the repumping scheme.

The advantage from using a repumping laser becomes clear, when we present the dark state formation of the system during the imaging process. To simulate the loss into the dark state g_5, we include only the light from the cooler beam and set this arbitrarily to an intensity of $I_{cool} = I_{sat}$. The resulting evolution is shown in Fig. 2.1a. The initial state is prepared in the ground state g_3 and evolves. We can observe the loss into the state g_5, which asymptotically approaches the maximal probability in circa $t_{exp} = 12\mu s$ and has a half value time of about $t_{exp} = 2\mu s$. This means that the imaged sample becomes transparent to the imaging light rather quickly and after this time no further investigation is possible. This illustrates the need for an additional laser, that shifts the populations back into the original resonant energy state and vice versa. The portrayed dynamics in Fig. 2.1b are computed under assumption of no detuning and an incoming flux of $I_{cool} = I_{rep} = I_{sat}$. The behaviour of the system can be described by stating, that after beginning in the initial state, the probability to find the atom in the corresponding excited state e_3 increases rapidly, is however superseded by the transfer into the secondary branch of g_5 and e_{13}, where an approximate steady state is reached at about $t_{exp} = 6\mu s$. At this point no more significant changes take place and the populations sustain a constant value. This proves in theory the idea behind a repumping laser. It should be mentioned that the name *repumper* is in some sense misleading, as it does not

---

[1] The used code is linked here: `https://github.com/finnscm/bachelor-thesis-code-LME-.git`

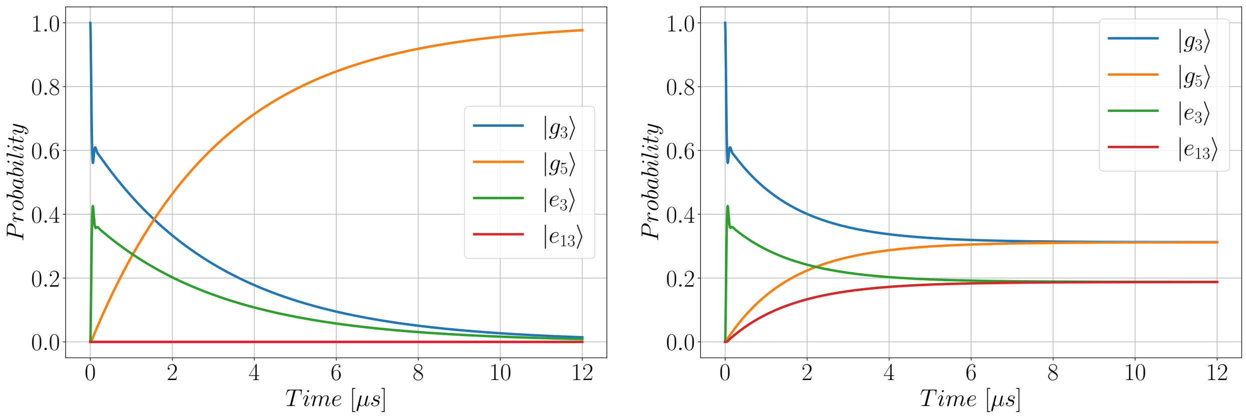

(a) *Dark state formation during imaging.* **(b)** *Evolution with addition of repumping laser.*

Figure 2.1: ***Evolution of populations in imaging scheme.*** *Temporal evolution of four-level system using numerical integrators for Lindblad master equation. In 2.1a evolutions were calculated using $I_{rep} = I_{sat}$. For the second figure 2.1b $I_{rep} = I_{cool} = I_{sat}$ were used to compute the populations. The benefit from adding a secondary laser* (**b**) *is clear due to constant non-zero steady states of the excited states, as the populations are proportional to the number of scattered photons, when comparing to* (**a**).

only transfer the lost atoms back into the primary imaging branch, but further serves as a secondary imaging light.

2.2 Number of Scattered Photons

With these simulations at hand, we have a powerful tool to make predictions for the experiment, e.g. we can calculate the number of scattering processes N_{sc}, which is the optimal parameter to optimize the ratio between the cooler and repumper light. To this end we must find a measure that contains information about the number of incoherent scattering events, that take place. We can do this by defining an appropriate measure $\mu(t)$ to be:

$$\mu(t) = \sum_j \Gamma_j \rho_{e_j e_j}(t) \tag{2.1}$$

Hence the scattering number N_{sc} is the integral of this measure over time, which is logical, as the decay of an excited state of the atom, corresponds to a previous scattering event, which populated said state:

$$N_{sc} = \int_0^{t_{exp}} \mu(t) \ dt = \int_0^{t_{exp}} \sum_j \Gamma_j \rho_{e_j e_j}(t) \ dt \tag{2.2}$$

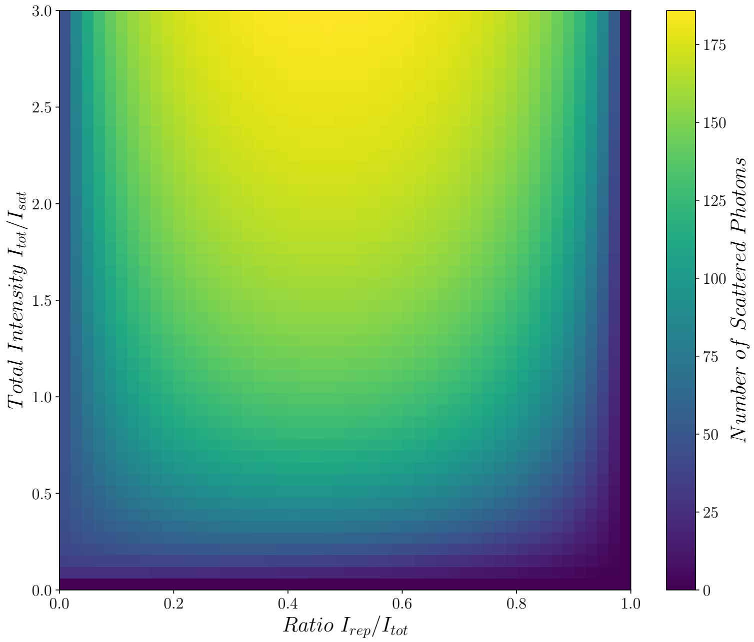

Figure 2.2: ***Simulation on number of scattered photons for different ratios between I_{cool} and I_{rep}.*** *Calculations are performed by integrating the Lindblad equation for a given combination of light intensities, which is used to compute the number of scattered photons (Eq. 2.2). The formation of a broad plateau is visible, with a slight asymmetry due to the initial preparation of the atoms in $|g_3\rangle$. An approx. optimal ratio between both light sources is given by equal contributions.*

The resulting plot is presented in Fig. 2.2 and was calculated for an exposure time of $t_{exp} = 12\mu s$. From the simulation we can now extract information on the optimal ratio between the two imaging light and observe, where the saturation plateau of the medium begins. The former reflects the symmetry of the closed atomic energy structure, which implies that an optimal ratio between I_{cool} and I_{rep} is reached at approximately equal contribution. Furthermore, we can distinguish the limits of the ratio between both light beams. On the one hand we have at $I_{cool} = I_{tot}$ some scattering, which manifests our notion, that we begin the simulation in ground state $|g_3\rangle$. In other words, if the ratio is $r = 0$ we recover the dark state formation scenario, where scattering events do occur until all populations are shifted into the secondary ground state $|g_5\rangle$. The second boundary is $I_{rep} = I_{tot}$, where no scattering events do and can take place, since there are no atoms prepared in the according state, that would allow for resonant interactions with light. We conclude, that the predictions of the simulations agree with our expectations on the system, that are motivated from symmetry arguments. Despite that, the central result we can take from Fig. 2.2 is the optimal and approximately equal ratio between both imaging beams, which is accompanied by a broad saturation plateau, that allows for a range of *good* ratios.

2.3 Effective Saturation Intensity

For now we have reduced the saturation intensity to the two-level system value $I_{\text{sat}} = 1.75 mW/cm^2$. This however is a strong assumption, which can easily be proven to be wrong, e.g. for an unbalanced contribution of both light beams in the closed imaging system (Fig. 1.6). Therefore it is necessary to define an effective saturation intensity $I_{\text{sat}}^{\text{eff}}$. The saturation intensity is typically defined as the intensity at which the absorption coefficient drops to half its value. This translates in case of the two-level system to the before mentioned numerical value for I_{sat}. We can however provide an estimate for the effective saturation intensity $I_{\text{sat}}^{\text{eff}}$ of the imaging system, by comparing when the number of scattered photons of the four-level system reaches the same value, as for the two-level system at its saturation intensity for a given exposure time. The corresponding intensity value, will show by which factor I_{sat} has to be scaled. This

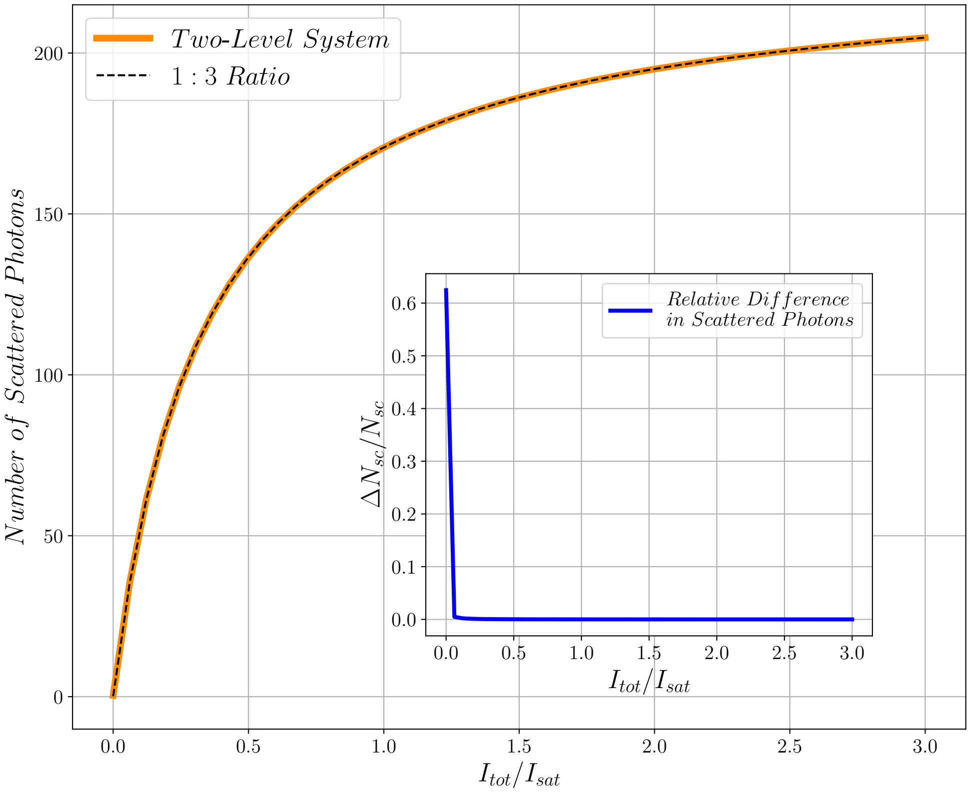

Figure 2.3: ***Scale adjusted four-level system.*** *The portrayed figure shows the number of scattered photons plotted against the incident light intensity. The solid line represents the two-level system and dashed line is the scaled four-level system with 1:3 ratio in light intensity. Both are integrated for* $12\mu s$ *exposure time and the steady state limit is employed. The inset shows that for* $I_{\text{sat}}^{\text{eff}} = 2.67\, I_{sat}$ *the systems coincide almost perfectly, such that the difference in scattered photons is relatively small.*

has been done in Fig. 2.3. We found a value of $I_{\mathrm{sat}}^{\mathrm{eff}} \approx 2\, I_{sat}$, while using an equal ratio between the binary laser system. Thus by scaling the total intensity by a factor of 2, we are able to reduce the four-level system to a two-level system. For the calculations we used the steady state limit. For other ratios such as $1:3$, where it does not matter which value corresponds to which light beam, because the system becomes fully symmetric in the used limit, we obtain $I_{\mathrm{sat}}^{\mathrm{eff}} \approx 2.67\, I_{sat}$. For a very unbalanced ratio of $1:9$ we yield $I_{\mathrm{sat}}^{\mathrm{eff}} \approx 5.5\, I_{sat}$. This means, that we can identify our closed imaging system with a saturation intensity adjusted two-level system by defining $I_{\mathrm{sat}}^{\mathrm{eff}}$ for a given ratio. It should be noted, that for this identification to be valid we must have a separation of time scales, i.e. the initial oscillation time of the system must be smaller, than the time needed for the time derivative of the populations to vanish.

Chapter 3

Experimental Imaging Results

3.1 Image Processing

In the experiment we use a charge coupled device (CCD) camera to obeserve the atomic cloud. The camera is a Princeton Instruments ProEM^{TM}and is the central measuring device in our setup. As all real semiconductors the individual pixels of the chip are no ideal measuring instruments, but rather exhibit thermal fluctuations and contain imperfections, that result in noise and a lower efficiency. Thus we must treat the device carefully and compensate for these characteristics. Especially, not every photon that hits the device is transformed via the photo-electric effect [20] into one single electron, also the absorption depends on the wavelength of the incident photon. The former phenomenon is associated with the quantum efficiency $QE(\lambda)$ of the camera, such that one photon can cause on average less than one photo-electron to be excited into the conduction band. Taking an image implies exposing the pixels during a specific amount of time to a flux of light, that causes electrons to be transferred into the conduction band. Since we are interested in the number of electrons per pixel, that have been created, readout electronics are used to amplify the accumulated charges pixel by pixel. The signal then is converted to a digital signal, that can be used for analysis. In this instance the term counts is used, which is a measure for the integrated electrons. Despite that there is no equivalence between the two, rather a linear relation, that is governed by the so-called gain g, which represents the proportionality factor, that ought to be determined to retrieve the photo-electron number, created in the imaging process. The readout procedure further adds to the total noise of the image. Because the analog-to-digital converter produces only positive values, an offset charge is added electronically to each pixel before conversion. This is subtracted from each images by the mean value of the image $I_{dark}(x, y)$, that exposes but does not open the cameras shutter to be hit by external photons. Furthermore debris and non-uniformity in the optical path will lead to interference patterns and shadows on the final image, which can be removed by taking a reference picture $I_{wo}(x, y)$ with full exposure, that doesn't include atoms, which we usually would want to observe in the atom picture $I_w(x, y)$.

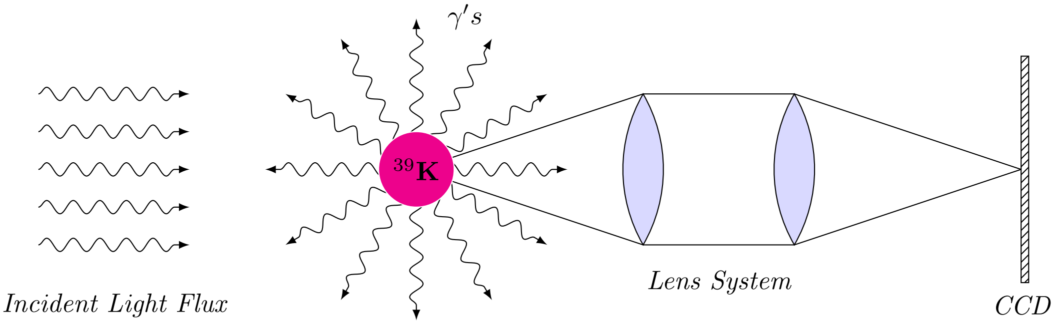

Figure 3.1: ***Simplified imaging setup.*** *The incident Light flux consisting of cooler and repumper light interacts with the trapped BEC. Due to resonant absorption and spontaneous decay of electrons only a small fraction of the initial light is captured via the lens system in the region of the condensate, which is surrounded by the non-absorbed light. Thus an absorption image is created on the CCD camera.*

The corrected picture can then be expressed via:

$$I_{cor}(x,y) = \frac{g}{QE(\lambda)} \cdot \frac{4\pi}{4\pi - \Omega} \cdot \left(n \cdot \left(I_{wo}(x,y) - \langle I_{dark}(x,y)\rangle\right) - \left(I_w(x,y) - \langle I_{dark}(x,y)\rangle\right)\right) \quad (3.1)$$

Here we assigned g to the gain of the CCD camera and Ω is the solid angle, which can be captured by the imaging lense. Since there can be differences in the total light intensities, we must normalize the reference image I_{wo} on the picture with atoms I_w. This is done by selecting a region around the region of interest (ROI) in both images, which is box-shaped and approximately $100px$ wide, subtracting the offset and summing over said area and dividing the resulting values in the following manner:

$$n = \frac{\sum_{x,y} I_w(x,y) - \langle I_{dark}(x,y)\rangle}{\sum_{x,y} I_{wo}(x,y) - \langle I_{dark}(x,y)\rangle} \quad (3.2)$$

3.2 CCD Gain

Since the gain of the CCD is camera-specific, we must measure g to be able to make use of Eq. 3.1. But because this quantity can not be measured directly, we will discuss a possible technique of acquiring its value.

As mentioned in Sec. 3.1 there are various sources for uncertainties, which can be exploited to calculate the gain. First, we will define the signal of the CCD Image by S_C, which is measured in counts. The signal in electrons on the other hand is given by S_E. Furthermore, we introduce the total noise in the image by $\sigma_{tot,C}$ & $\sigma_{tot,E}$. The total noise consists of three main contributions, which are as discussed before the readout noise σ_R, but also pixel response non-uniformity σ_{PRNU} and photon shot noise σ_{SN}. By stating, that the different noise sources are independent of each other, we can apply Gaussian propagation of uncertainties, such that we yield [21]:

$$\sigma^2_{tot,E} = \sigma^2_{SN,E} + \sigma^2_{PRNU,E} + \sigma^2_{R,E} \tag{3.3}$$

As previously noted, the gain is simply the multiplying factor between counts and electrons, wherefore we can write:

$$S_E = g \cdot S_C \text{ and } N_E = g \cdot N_C, \tag{3.4}$$

where S is the recorded signal and N is the corresponding noise. It is especially important to note, that photon shot noise is Poisson distributed, because photonic detection is a random process, where light is considered as discretized quanta and interacts with the measuring device independently, this is logical. Therefore, we can express the probability distribution by:

$$P_\lambda(k) = \frac{\lambda^k}{k!}\mathrm{e}^{-\lambda} \tag{3.5}$$

Where λ is the expectation value, that assigns $k \in \mathbb{N}_0$ the probability P. A short calculation, will prove that the variance of any Poisson distribution is equivalent to the expectation value λ:

$$Var(X) = E\left(X^2\right) - (E(X))^2 = \lambda^2 + \lambda - \lambda^2 = \lambda \tag{3.6}$$

This remarkable result can be employed in Eq. 3.3. While also using Eq. 3.4 we can rearrange to:

$$N_C^2 = \frac{1}{g} S_C + (\sigma^2_{R,C} + \sigma^2_{PRNU,C}) \tag{3.7}$$

This means the gain is the inverse slope and can be measured via the count number. For the experiment, this means we are taking a set of images for a range of different intensities. More specifically we took ten images at a given intensity and repeated this for ten different intensities. As a light source we used an ordinary lamp, which was flat field adjusted, in such manner, that there were only minimal gradients and inhomogeneities. More specifically, this means that we placed white paper in front of the light source. This is done to scatter the lamps light more diffusely and suppress irregularities in the light signal, which are caused by light diffraction from the glass enclosure of the lamp. From each individual picture we calculated the variance in a squared box of length $20px$. The variance, which is averaged for each intensity, is then plotted against the number of mean counts in the square and a linear equation is fitted to the data points using the least square method. The corresponding graph is shown in Fig. 3.2. This *estimate* of g assumes the absence of flat field effects, since a slight curvature can be seen in Fig. 3.2. This especially implies a neglection and underestimation of contributions originating from σ_{PRNU}, which scales quadratically with the signal. A more precise measurement in the future would account for flat field effects. For now our best estimate is $g = 1.878 \pm 0.041$.

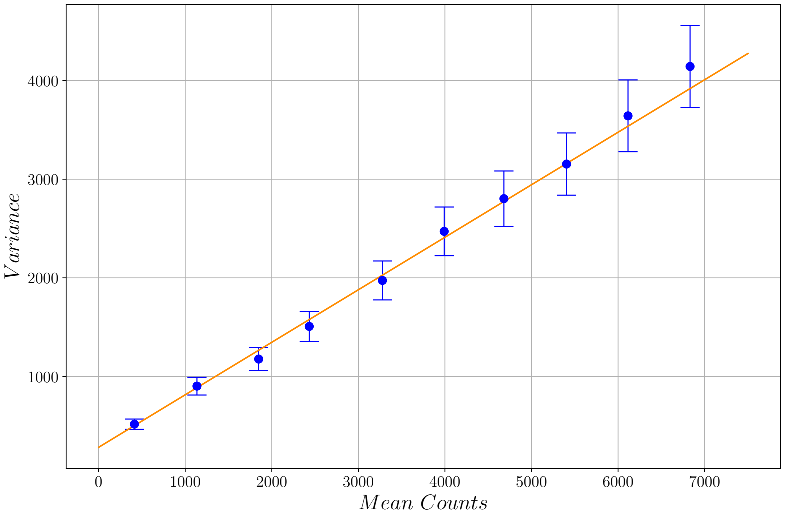

Figure 3.2: ***Gain estimation.*** *Using the method described in Sec. 3.2. The variance in signal is plotted against the mean counts in an approximately homogeneous square with a length of 20px. A linear function is fitted to the data points using the least square method. For the gain we find a value of* $g = 1.878 \pm 0.041$.

3.3 Dark State Formation and Repumping Laser

The loss phenomenon, caused by the superposition of I, J-states, will now be tested in the experiment, which is the experimental equivalent to Sec. 2.1. In order to illustrate the significance of the secondary laser we performed two measurements, where the usage of a repumping laser is compared to the use of a solitary laser imaging system. We expect to see a flattening of the curve in the latter scenario, whereas we suspect a longer regime, in which the number of scattered photons does not saturate as quickly, when considering the addition of the secondary laser, since this scenario is in theory a closed optical cycling scheme.

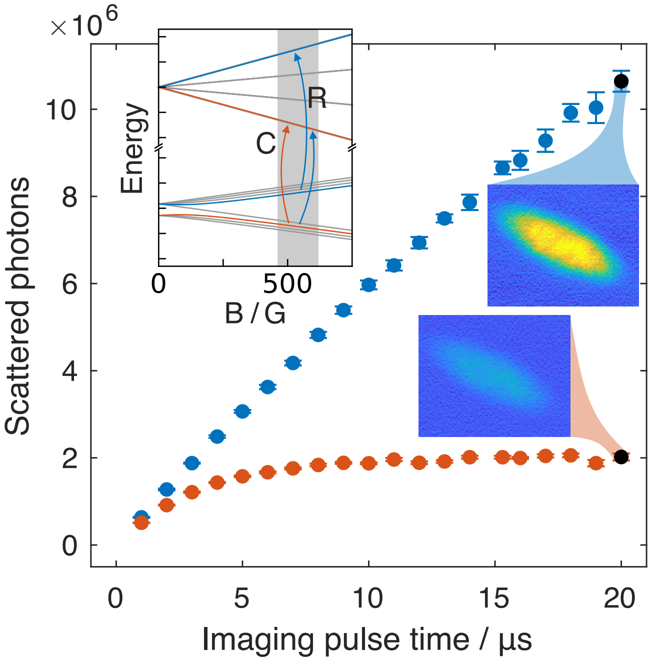

Figure 3.3: ***Number of scattered photons plotted against imaging pulse times.*** *Dark state formation is shown with fast saturation, when using the single cooler light beam (red). Imaging including the secondary repumping laser beam, the number of scattering events can be increased significantly (blue). The final image of the BEC is shown for both scenarios. The inset portrays the imaging scheme inside the energy structure, where C represents cooler and R repumping light.*

The corresponding behaviour is shown in Fig. 3.3, where both experiments meet our expectations. We can see, that a repumping laser significantly increases the possible imaging duration. Without this laser however, we can detect an asymptotic curvature, which fits nicely to our interpretation, that all populations are shifted into the dark state and thus become non-resonant. The curves begin to differ even for the smallest imaging pulse times, such that the employment of this technique is worthwhile for most imaging durations. Eventually the linear regime is superseded by a saturation plateau, which predominantly is caused by the momentum transfer of photons to the atomic cloud, which leads to the sample being blown out of focus.

3.4 Number of Scattered Photons

Finally we will optimize the ratio between I_{cool} and I_{rep}. A good measure is the number of scattered photons, as we want to enhance the absorption by the atomic cloud. In the experiment, we use AOMs to control the contribution of the light beams to the total imaging power. This ratio is then tuned from zero to one, where a value of one marks the point at which only I_{cool} is present. By repeating this procedure for different total intensities, we reproduce Fig. 2.2 experimentally.

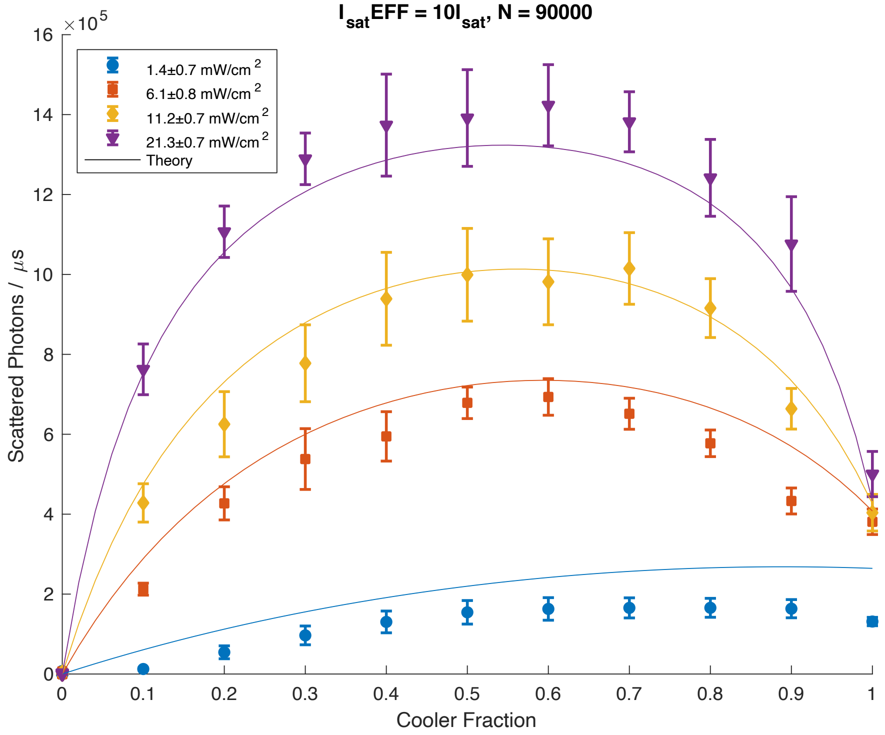

Figure 3.4: ***Number of scattered photons plotted against different imaging light ratios for different total intensities.*** *The imaging intensities are 3.6mW/cm^2 (blue circles), 6.1mW/cm^2 (red squares), 11.2mW/cm^2 (yellow diamonds), 21.3mW/cm^2 (purple triangles) and the solid lines are numerical solutions computed using results from Sec. 2.2 for the four level system. An optimal ratio was found to be* $r \approx 0.55$.

In Fig. 3.4 the described measurement are portrayed. As expected from theory, in a given intensity class the scattering events start at zero, since no cooler light implies no resonant light to be present that can be absorbed by the atoms. The optimal ratio is reached at $r \approx 0.55$. The number of scattered photons drops to a non-zero value, when only cooler light is present. This behaviour is clear, as we know that this case represents the dark state formation scenario, where the atoms are resonant initially and transfer into state $|g_5\rangle$. For larger intensities these characteristics repeat, with the only difference being, that the overall number of scattered photons rises. These findings agree with our simulations, where we could state similar results for the system. To the experimental data points we fitted lines, which are also shown in Fig. 3.4. Here a group of data points is fitted individually with the results from the simulation for a given intensity. The most compelling conclusion we can draw from this measurement is, that our assumption on the optimal ratio have been confirmed, such that we can say with confidence, that an approximate equipartition between the both light sources yields optimal absorption characteristics. A way to improve absorption even more might be by changing the intensities dynamically, in such a manner, that first the cooler constitutes the main light source, where the atoms are prepared in either way, followed by a gradual addition of repumper intensity. However, one should be reminded, that signal to noise is the most important quantity to maximize and therefore only increasing scattering events will not suffice.

3.5 Atom Number

Finally, we want to give an outlook on a possibility for measuring the absolute number of atoms in the condensate. To do so, we have to calibrate our imaging system in order to obtain correct spatial optical densities $n(x, y, z)$. One calibration method is given by [22], which we will use in the following. The Lambert-Beer law, which describes absorption processes can be applied here by accounting for saturation effects:

$$\frac{dI}{dz} = -n\frac{\sigma_0}{\alpha^*}\frac{1}{1 + I/I_{\text{eff}}^{\text{sat}}}I \equiv -n\sigma(I)I \tag{3.8}$$

Here I is the incident light beams intensity, $\sigma_0 = 3\lambda^2/2\pi$ the resonant cross section and $I_{\text{eff}}^{\text{sat}} = \alpha^* I_{\text{sat}}$ the effective saturation intensity, which depends on the saturation intensity, here $I_{\text{sat}} = 1.75\text{mW/cm}^2$. Form this equation we can derive the optical depth and define it by:

$$od_0(x, y) \equiv \sigma_0 \int n(x, y, z)dz = f\left(x, y; \alpha^*\right) \tag{3.9}$$

where the function $f(x, y, \alpha^*)$ is given by:

$$f\left(x, y; \alpha^*\right) = -\alpha^* \ln\left(\frac{I_{\text{f}}(x, y)}{I_{\text{i}}(x, y)}\right) + \frac{I_{\text{i}}(x, y) - I_{\text{f}}(x, y)}{I_{\text{sat}}} \tag{3.10}$$

Here we define $I_{\text{i}}(x, y) = I_{\text{wo}}(x, y) - \langle I_{\text{dark}}(x, y)\rangle$ and $I_{\text{f}}(x, y) = I_{\text{w}}(x, y) - \langle I_{\text{dark}}(x, y)\rangle$. The logarithmic term in Eq. 3.10 can be identified with the optical density $\delta_0(x, y)$. Now the crux of this calibration is to find an optimal parameter α^* at which the standard deviation of the optical depth $\Delta(od)$ is minimized. Experimentally this means, one has to calculate the *od* for varying initial light intensities and try different α's. For each tested α the standard deviation $\Delta(od)$ is calculated, until one finds the value of α for which $\Delta(od)$ is minimal. Specifically this means, that the an α^* has to be found for which the two terms in Eq. 3.9 add up to a constant value, which then is the calibrated optical depth. However, this method assumes a two-level system, which in our experiment is not the case. Nonetheless, as we have shown in Sec. 2.3 we can reduce our imaging scheme to the two-level system by adjusting the saturation intensity, provided that imaging times are long enough, such that the steady state solutions become a good approximation. Hence this scaling can be incorporated in the parameter α^*.
From the calibrated densities, we can now determine the number of atoms. In the experiment we take images in the described way of Sec. 3.1, where we use high light intensities, such that the imaging is nearly linear even for higher densities. The resulting density distribution is then compared to numerical values from the Gross-Pitaevskii equation, where the number of atoms is varied. The simulation of the density distribution, which fits best to our data, then contains our estimate for the number of atoms in the atomic sample. In case of a harmonic trap, we have to calibrate the magnification of the lens system (Fig. 3.1) and measure the trapping frequency [23].

Conclusion

In conclusion, we have analyzed the imaging system used to investigate ultra-cold potassium $^{39}\mathbf{K}$ atoms. We refined the theoretical framework, that is used to describe interactions between light quanta and atomic clouds. In this context we presented a closed optical cycle imaging technique. This method uses a binary laser system, that compensates for loss effects due to a non-pure energy structure. Further, we performed simulations, that used the Lindblad master equation to optimize scattering events during the imaging process. Finally, we compared our theory to experimental data and elaborated on how images are processed to obtain quantitative results.

(i) Since the isotope $^{39}\mathbf{K}$ has a broad Feshbach resonance at $B = 562G$ we argued for this atom species as a suitable subject for investigation. We demonstrated, that in the intermediate magnetic field regime, we have decay modes, that have not been considered previously. In order to quantify these decay channels, we calculated the dipole matrix elements by exploiting the Wigner-Eckart theorem. We derived a general expression for the dipole matrix elements for alkali metals, that was evaluated for the used potassium isotope (Fig. 1.4). The predominant result here is, that the decays strongly depend on the applied external magnetic field. Therefore the consideration of these decay modes becomes important for any alkali metal in the respective intermediate field regime.

(ii) For our open dissipative system we build the Hamiltonian in the interaction frame in order to construct the Lindblad master equation. From the resulting Maxwell-Bloch equation we could quantify the loss phenomenon using the evolution of the populations. Together with the dipole matrix elements, we argued for the existence of a closed cycle imaging system, that utilizes a binary laser setup. For this scheme we were able to argue for the benefits of adding the secondary laser, which suppressed the dark state formation (Fig. 2.1b).

(iii) Since a second laser directly poses the question of an optimal ratio in intensity between both frequencies, we optimized this parameter numerically. Specifically we found that by using the number of scattered photons as measure for good absorption characteristics of the atomic medium we could optimize the contributions well. We found from these simulations (Sec. 2.2) that the optimal ratio is given at approximately equal ratio. Furthermore we could detect a slight asymmetry here, which is a manifest to the initial condition, such that the primary laser light scatters more, since the medium is prepared in its resonant state. These findings were substantiated from experimental results. Experimentally a contribution of $r \approx 0.55$ of the cooler light showed optimal scattering properties. Moreover the previously found asymmetry was reproduced in the experiment (Fig. 3.4).

(iv) Finally, we provided a brief description on a method for calibrating the imaging system and determining the number of atoms in the medium. In this context we were able to reduce the four-level system to an effective two-level system by employing the steady state approximation. Furthermore we defined an effective saturation intensity for the atomic cloud $I_{\text{sat}}^{\text{eff}}$. This quantity allowed to scale the number of scattered photons in dependence of the incident light intensity identically to an effective two-level system (Fig. 2.3). The implications are, that if we define a new saturation intensity for our imaging scheme we can calibrate our system equivalently to a two-level system, provided that imaging times are longer than the initial oscillations in populations, i.e. that the steady states are reached quickly.

References

[1] T.W. Hänsch and A.L. Schawlow. “Cooling of gases by laser radiation”. In: *Optics Communications* 13.1 (Jan. 1975), pp. 68–69. DOI: `10.1016/0030-4018(75)90159-5`. URL: `https://doi.org/10.1016/0030-4018(75)90159-5`.

[2] M. H. Anderson et al. “Observation of Bose-Einstein Condensation in a Dilute Atomic Vapor”. In: *Science* 269.5221 (July 1995), pp. 198–201. DOI: `10.1126/science.269.5221.198`. URL: `https://doi.org/10.1126/science.269.5221.198`.

[3] K. B. Davis et al. “Bose-Einstein Condensation in a Gas of Sodium Atoms”. In: *Physical Review Letters* 75.22 (Nov. 1995), pp. 3969–3973. DOI: `10.1103/physrevlett.75.3969`. URL: `https://doi.org/10.1103/physrevlett.75.3969`.

[4] Chiara D’Errico et al. “Feshbach resonances in ultracold39K”. In: *New Journal of Physics* 9.7 (July 2007), pp. 223–223. ISSN: 1367-2630. DOI: `10.1088/1367-2630/9/7/223`. URL: `http://dx.doi.org/10.1088/1367-2630/9/7/223`.

[5] Sebastian Erne et al. “Universal dynamics in an isolated one-dimensional Bose gas far from equilibrium”. In: *Nature* 563.7730 (Nov. 2018), pp. 225–229. DOI: `10.1038/s41586-018-0667-0`. URL: `https://doi.org/10.1038/s41586-018-0667-0`.

[6] G. Gauthier et al. “Direct imaging of a digital-micromirror device for configurable microscopic optical potentials”. In: *Optica* 3.10 (Oct. 2016), p. 1136. ISSN: 2334-2536. DOI: `10.1364/optica.3.001136`. URL: `http://dx.doi.org/10.1364/OPTICA.3.001136`.

[7] Walter Greiner, Ludwig Neise and Horst Stöcker. *Thermodynamics and Statistical Mechanics*. Springer New York, 1995. DOI: `10.1007/978-1-4612-0827-3`. URL: `https://doi.org/10.1007/978-1-4612-0827-3`.

[8] J. Rogel-Salazar et al. “Methods of quantum field theory for trapped Bose–Einstein condensates”. In: *Journal of Optics B: Quantum and Semiclassical Optics* 6 (Sept. 2004), R33–R59. DOI: `10.1088/1464-4266/6/9/R01`.

[9] T. G. Tiecke. *Feshbach resonances in ultracold mixtures of the fermionic quantum gases 6Li and 40K*. PhD thesis, University of Amsterdam, 2009.

[10] Cheng Chin et al. “Feshbach resonances in ultracold gases”. In: *Reviews of Modern Physics* 82.2 (Apr. 2010), pp. 1225–1286. ISSN: 1539-0756. DOI: `10.1103/revmodphys.82.1225`. URL: `http://dx.doi.org/10.1103/RevModPhys.82.1225`.

[11] Charles Schwartz. “Theory of Hyperfine Structure”. In: *Physical Review* 97.2 (Jan. 1955), pp. 380–395. DOI: `10.1103/physrev.97.380`. URL: `https://doi.org/10.1103/physrev.97.380`.

[12] M. Inguscio E. Arimondo and P. Violino. “Experimental determinations of the hyperfine structure in the alkali atoms”. In: *Physical Review A* 49(1):31–75.1 (Jan. 1977). DOI: 10.1.1.701.5018.

[13] A. Hebecker. *Quantenmechanik, Vorlesungsnotizen zum Kurs von A. Hebecker, Sommersemester 2018 und 2019*. available online at https://www.thphys.uni-heidelberg.de/~hebecker/QM/qm.pdf.

[14] P. Zeeman. “The Effect of Magnetisation on the Nature of Light Emitted by a Substance”. In: *Nature* 55.1424 (Feb. 1897), pp. 347–347. DOI: 10.1038/055347a0. URL: https://doi.org/10.1038/055347a0.

[15] Arno Bohm. “Addition of Angular Momenta—The Wigner-Eckart Theorem”. In: *Quantum Mechanics: Foundations and Applications*. Springer Berlin Heidelberg, 1986, pp. 164–204. DOI: 10.1007/978-3-662-01168-3_5. URL: https://doi.org/10.1007/978-3-662-01168-3_5.

[16] Daniel A. Steck. *Quantum and Atom Optics*. available online at http://steck.us/teaching (revision 0.13.3, 10 June 2020).

[17] A. R. Edmonds. *Angular Momentum in Quantum Mechanics*. Princeton University Press, Dec. 1957. DOI: 10.1515/9781400884186. URL: https://doi.org/10.1515/9781400884186.

[18] B. Erdmann. *Wechselwirkung von atomaren Mehrniveau-Systemen mit Laserlicht*. Bachelor’s thesis. University of Heidelberg (2019).

[19] Carlos Alexandre Brasil, Felipe Fernandes Fanchini and Reginaldo de Jesus Napolitano. “A simple derivation of the Lindblad equation”. In: *Revista Brasileira de Ensino de Física* 35.1 (Mar. 2013). ISSN: 1806-1117. DOI: 10.1590/s1806-11172013000100003. URL: http://dx.doi.org/10.1590/S1806-11172013000100003.

[20] A. Einstein. “Über einen die Erzeugung und Verwandlung des Lichtes betreffenden heuristischen Gesichtspunkt”. In: *Annalen der Physik* 322.6 (1905), pp. 132–148. DOI: 10.1002/andp.19053220607.

[21] Michael Newberry. *Tech Note: Pixel Response Effects on CCD Camera Gain Calibration*. available online at https://www.mirametrics.com/tech_note_ccdgain.php.

[22] G. Reinaudi et al. “Strong saturation absorption imaging of dense clouds of ultracold atoms”. In: *Optics Letters* 32.21 (Oct. 2007), p. 3143. ISSN: 1539-4794. DOI: 10.1364/ol.32.003143. URL: http://dx.doi.org/10.1364/OL.32.003143.

[23] Ketterle W., Durfee D.S. and Stamper-Kurn D.M. “Making, probing and understanding Bose-Einstein condensates”. In: *Proceedings of the International School of Physics "Enrico Fermi"* 140.Bose-Einstein Condensation in Atomic Gases (1999), pp. 67–176. ISSN: 0074-784X. DOI: 10.3254/978-1-61499-225-7-67. URL: https://doi.org/10.3254/978-1-61499-225-7-67.

Acknowledgements

Im Folgenden möchte ich mich bei allen bedanken, die mich bei dieser Arbeit unterstützt haben.

Dazu bedanke ich mich herzlich bei Prof. Markus Oberthaler. Markus schafft es mit seinem Wissensdrang und seiner Kreativität immer wieder aufs Neue Faszination für moderne Forschung auszulösen, die ansteckend ist.

Ich freue mich auch deshalb sehr darüber, dass er mich in seiner Arbeitsgruppe aufgenommen hat.

Mein Dank gilt vorallem auch meiner Arbeitsgruppe, dem BECK mit Celia, Helmut, Marius, Maurus und Nikolas. Ihr bildet ein harmonisches Umfeld, in dem man sich wohlfühlt. Ihr hattet immer ein offenes Ohr für meine Ideen und Probleme und habt mir eine Menge beigebracht.

Besonders habt ihr mich auch bei dieser Arbeit unterstützt, eure Kritik und Verbesserungsvorschläge waren immer willkommen und haben diese Arbeit geprägt.

In diesem Zuge möchte ich mich auch bei Dr. Martin Gärttner bedanken, der mich in der Theorie und den Simulationen unterstützt hat.

Auch möchte ich Prof. Selim Jochim danken, der sich bereiterklärt hat Zweitprüfer dieser Arbeit zu sein.

Erklärung

Ich versichere, dass ich diese Arbeit selbstständig verfasst und keine anderen als die angegebenen Quellen und Hilfsmittel benutzt habe.

Heidelberg, den 27. Oktober 2020,

Finn Schmatke